J. Fluid Mech. (1996), *vol.* 307, *pp.* 11–41

Unsteady behaviour of a topography-modulated tripole

By O. U. VELASCO FUENTES†, G. J. F. VAN HEIJST AND N. P. M. VAN LIPZIG
Fluid Dynamics Laboratory, Eindhoven University of Technology, PO Box 513,
5600 MB Eindhoven, The Netherlands

(Received 12 December 1994 and in revised form 9 September 1995)

The evolution of a tripolar vortex under the influence of a parabolic topography – like the free surface of a rotating fluid – is studied experimentally and with a point-vortex model. Laboratory experiments reveal that tripoles generated off-axis become asymmetric and the whole structure travels towards the centre of the tank along an anticyclonic spiral. During this translation the structure rotates quasi-periodically with the core pairing alternately with one of the satellites. An asymmetric point-vortex tripole (with the central vortex located at a distance ϵ from the middle point of the configuration) displays a periodic motion which is qualitatively similar to the motion of the laboratory tripoles. The exchange of fluid between the three vortices as a function of the perturbation parameter ϵ is studied using the lobe-dynamics technique. A point-vortex tripole modulated on the basis of conservation of potential vorticity reproduces quantitatively the trajectories of the individual vortices measured in the laboratory. As in the experiments, the model shows that fluid is strongly stirred in the region surrounding the vortex cores and that the tripole carries a finite amount of fluid.

1. Introduction

Two-dimensional flows are characterized by the emergence of coherent long-lived vortices. Among these, the most abundant vortex types are the monopole, which consists of a region of fluid rotating around a single centre, and the dipole, which is a self-propagating arrangement of two closely attached monopoles of opposite sign. The tripolar vortex follows the monopole and the dipole in increasing order of complexity. This vortex structure can be defined as a compact, linear arrangement of three patches of continuously distributed vorticity, with the central vortex being flanked at its longer sides by two weaker vortices of oppositely signed vorticity. This symmetric configuration performs, as a whole, a steady rotation in the direction defined by the circulation of the central vortex.

The emergence of a symmetric tripole from an unstable monopolar vortex was originally mentioned by Leith (1984), who subjected a minimum-enstrophy vortex to a random asymmetric perturbation. This transition has been observed later both in laboratory experiments (van Heijst & Kloosterziel 1989; van Heijst, Kloosterziel & Williams 1991; Flór *et al.* 1993) and in numerical simulations (Carton, Flierl &

---

† Present affiliation: CICESE, Departamento de Oceanografía Física, 22800 Ensenada, B.C., México.

Polvani 1989; Orlandi & van Heijst 1992). Tripoles have also been observed to arise spontaneously in two-dimensional turbulent flows (Legras, Santangelo & Benzi 1988) and by a collision of two misaligned dipolar vortices (Orlandi & van Heijst 1992). Recently, a tripolar-like vortex has been observed in the ocean in the Gulf of Biscay (Pingree & LeCann 1992). In this case the tripolar structure – visible in sea-surface temperature – consisted of an elongated anticyclonic central vortex and two smaller cyclonic satellites and it had a horizontal dimension of 50–60 km.

Van Heijst *et al.* (1991) studied the generation process of the tripolar vortex in a rotating homogeneous fluid from the instability of a cyclonic vortex, and the further evolution of the symmetric tripole. They compared flow measurements (stream function and vorticity distribution) with a point-vortex tripole and found that the main features shown by the laboratory tripole, namely the overall rotation of the structure and the topology of the streamlines in the co-rotating frame, are well described by the model. Flór *et al.* (1993) observed the emergence of a tripolar vortex from the instability of a monopolar vortex generated in a non-rotating linearly stratified fluid. This tripole, however, existed only for a short period before the destruction of the satellites and the subsequent transformation of the structure into a new monopolar vortex.

Carton *et al.* (1989) studied numerically the instability of isolated monopolar vortices (i.e. monopoles with both positive and negative vorticity but zero net circulation) subjected to a mode-2 perturbation and found that the evolution depends on the steepness of the vorticity profile. For vorticity gradients in an intermediate range the monopolar instability leads to the formation of a tripolar vortex. A similar study was done by Orlandi & van Heijst (1992), who prescribed a random perturbation and observed that the mode-2 component dominated the evolution. This scenario is in agreement with the experimental situation, where the vorticity profile is smooth and – because of the generation mechanism – it is to be expected that the perturbations do not contain any preferred mode, but the most unstable one finally dominates (van Heijst *et al.* 1991).

The tripole has been observed to be a steady and stable structure both experimentally and numerically: it can exist for many rotation periods without noticeable change of shape or size. However, it has been observed recently that a tripole generated off-axis in a rotating fluid rapidly loses its symmetry and the individual vortices show a complicated quasi-periodic motion (van Heijst & Velasco Fuentes 1994). This behaviour produces a continuous stretching and folding of (dyed) fluid patches initially located within the tripole, a feature that suggests the existence of chaotic motion of fluid particles. A similar unsteady motion of the vortex centres has been observed in numerical simulations by Carton & Legras (1994), although in their case the unsteady motion and the asymmetry appear gradually after several rotations of the structure.

The observation that quasi-periodic motion rapidly arises when the tripole is generated off-axis, as well as the numerical experiments showing the steadiness over a long period of the tripole in the two-dimensional case, suggest that the cause of the unsteady behaviour is a three-dimensional effect. The parabolic free surface of the rotating fluid produces a continuous stretching and squeezing of the vortex columns, which must change strength in order to preserve potential vorticity. This 'modulation' of the vortex strengths due to the non-uniform fluid depth is put forward here as the mechanism that causes the asymmetry and propagation of the tripole.

The dynamic effect of the non-uniform depth produced by the parabolic free surface is equivalent to that of the so-called γ-plane, which models the distribution of ambient vorticity close to the pole of a rotating planet (see e.g. Nof 1990). In this connection, it is worth mentioning the complicated dynamics of isolated monopoles on the β-plane (which models the mid-latitude distribution of vorticity). As described by Carnevale, Kloosterziel & van Heijst (1991) and Sutyrin *et al.* (1994), in this case the evolution of the vortex is influenced by two intrinsic tendencies: (*a*) the mode-2 instability with the subsequent transformation into a tripolar vortex, and (*b*) the vortex drift – northwestwards for a cyclonic vortex in the northern hemisphere – usually accompanied by Rossby wave radiation. These authors did not presented details about the complicated motion of the satellites around the core or about mass transport between flow regions.

This paper is organized as follows. In §2 we discuss the typical evolution of a tripole in a rotating-tank experiment. Section 3 is devoted to the motion of the vortex centres we use first a non-modulated point-vortex tripole, which is shown to display some features observed in the experiments, and later we analyse the modulated case and compare results with laboratory observations. Section 4 deals with the advection of fluid particles in the point-vortex models: here we present a comparison of the evolution of dye patterns in the laboratory and passive contours in the modulated point-vortex model. In §5 we summarize the results and give some conclusions.

2. Laboratory observations of an unsteady tripole

For the motion of a shallow layer of inviscid homogeneous fluid rotating at a constant angular speed Ω one may derive the conservation relation (e.g. Pedlosky 1979)

$$\frac{\mathrm{D}}{\mathrm{D}t}\left(\frac{\omega+f}{h(x,y)}\right)=0, \tag{2.1}$$

where $\mathrm{D}/\mathrm{D}t \equiv \partial/\partial t + \boldsymbol{u}\cdot\nabla$ is the material derivative in two dimensions – with $\boldsymbol{u}$ the horizontal velocity, ω is the vertical component of the relative vorticity $\boldsymbol{\omega} \equiv \nabla\times\boldsymbol{u}$, $f = 2\Omega$ is the Coriolis parameter, and $h(x,y)$ is the fluid depth. Owing to the system's rotation the free surface of the fluid acquires a parabolic shape. Since the bottom is assumed to be flat, the depth as a function of position is given by $h(y) = h_0[1+f_0^2r^2/(8gh_0)]$, with g the gravity acceleration and r the distance to the rotation axis, at which the fluid has a depth h_0. By substituting this expression in (2.1) and expanding the result in a Taylor series one obtains

$$\frac{\mathrm{D}}{\mathrm{D}t}\left(\omega-\frac{f^3r^2}{8gh_0}\right)=0, \tag{2.2}$$

where a small Rossby number ($\omega/f_0 \ll 1$) is assumed and second-order terms have been neglected.

Let us now consider the case of a layer of fluid with constant depth h_0 located close to the pole of a rotating planet. The horizontal dimensions are assumed to be small compared to the planet's radius, so that the curvature of the domain enters (2.1) only through the variation of the Coriolis parameter, which in this case is given by $f = 2\Omega\sin\phi$, where ϕ is the geographical latitude. A Taylor expansion of the latter expression around the pole ($\phi = \frac{1}{2}\pi$) renders the linear term (β) identically zero and the Coriolis parameter is given to leading order by $f = f_0 - \gamma r^2$, where $f_0 = 2\Omega$ and $\gamma = \Omega/R^2$, with R the planet's radius. This approximation is known as the γ-plane model (Nof 1990) and leads to the following expression for conservation of potential vorticity:

$$\frac{\mathrm{D}}{\mathrm{D}t}(\omega - \gamma r^2) = 0, \tag{2.3}$$

where r is now the distance to the pole. Equations (2.2) and (2.3) are equivalent, showing that the dynamics of a free-surface rotating fluid is equivalent to that of a fluid on a γ-plane, with the 'topographic' γ given by $\gamma = f^3/8gh_0$. Note that *north* is equivalent to *shallow*, and lines of equal fluid depth (isobaths) correspond with lines of equal latitude (parallels).

The experiments were carried out in a rectangular tank of horizontal dimensions 100×150 cm^2 and 30 cm depth mounted on a rotating table, with the tank's centre located at the rotation axis. The angular speed of the system was set to $\Omega = 0.56$ s^{-1}, so that the Coriolis parameter $f = 1.12$ s^{-1}, and – in the experiment described below – the tank was filled up to a height of $h_0 = 17$ cm. Therefore the parabolic free surface produced a value of $\gamma = f^3/8gh_0 = 0.109$ m^{-2}s^{-1}. The difference in water depth between the axis of rotation and the closest walls was 4 mm.

A tripolar vortex was generated by stirring the fluid cyclonically in a bottomless cylinder of 19 cm internal diameter, placed in the rotating fluid at 30 cm from the rotation axis, and then quickly lifting this cylinder. The flow was visualized using fluorescein, which was added to the fluid after stirring it and before the generating cylinder was removed. An isolated monopole (i.e. a vortex with a single rotation centre and zero net circulation) was thus produced in the uniformly rotating ambient fluid. This vortex became unstable, resulting in the gradual formation of a tripolar vortex. When the formation process of the tripole was completed (figure 1*a*) the three vortices were aligned and the two satellites were located at equal distances from the central vortex. The structure rotated as a solid body and, owing to the off-centre location of the tripole, the satellites were alternately squeezed and stretched as they rotated around the central vortex. Note that in this particular experiment the satellites encountered a difference of about 1.5 mm in fluid depth between their locations of minimum (20 cm) and maximum (40 cm) separation form the tank centre. This seemingly small value turned out to have a major effect on the evolution of the structure. After about one rotation of the satellites, a small asymmetry began to develop and the vortices lost their alignment (figure 1*b*) and the central vortex then moved away with one of the satellites (figure 1*c*). However, this couple was asymmetric and moved along a curved trajectory (figure 1*d*). As a result of the collision of the couple with the satellite left behind (figure 1*e*) the central vortex changed partner and the new couple moved away. Then the process repeated itself, with the subsequent looping excursion of the couple being larger (compare figures 1*g* and 1*e*), and with the vortices being arranged in an almost right-angled triangle during the collision of the couple with the satellite (figure 1*i*).

Another remarkable feature observed in this experiment is the complicated distribution of dye. Each time the central vortex pairs with one of the satellites, the new couple leaves behind a tail of dye that links it with the remaining satellite (figure 1*c*). As the couple returns, the tripolar structure traps the ambient (undyed) fluid located between the couple, the satellite and the tail of dyed fluid (figure 1*d*). Subsequently, as the central vortex changes partner, this ambient fluid is wrapped around the new couple (figure 1*e*). This process, which occurs every time the central vortex changes partner, leads to the formation of alternating filaments of dyed and undyed fluid, as is revealed by a close examination of the tail linking the couple with the monopole

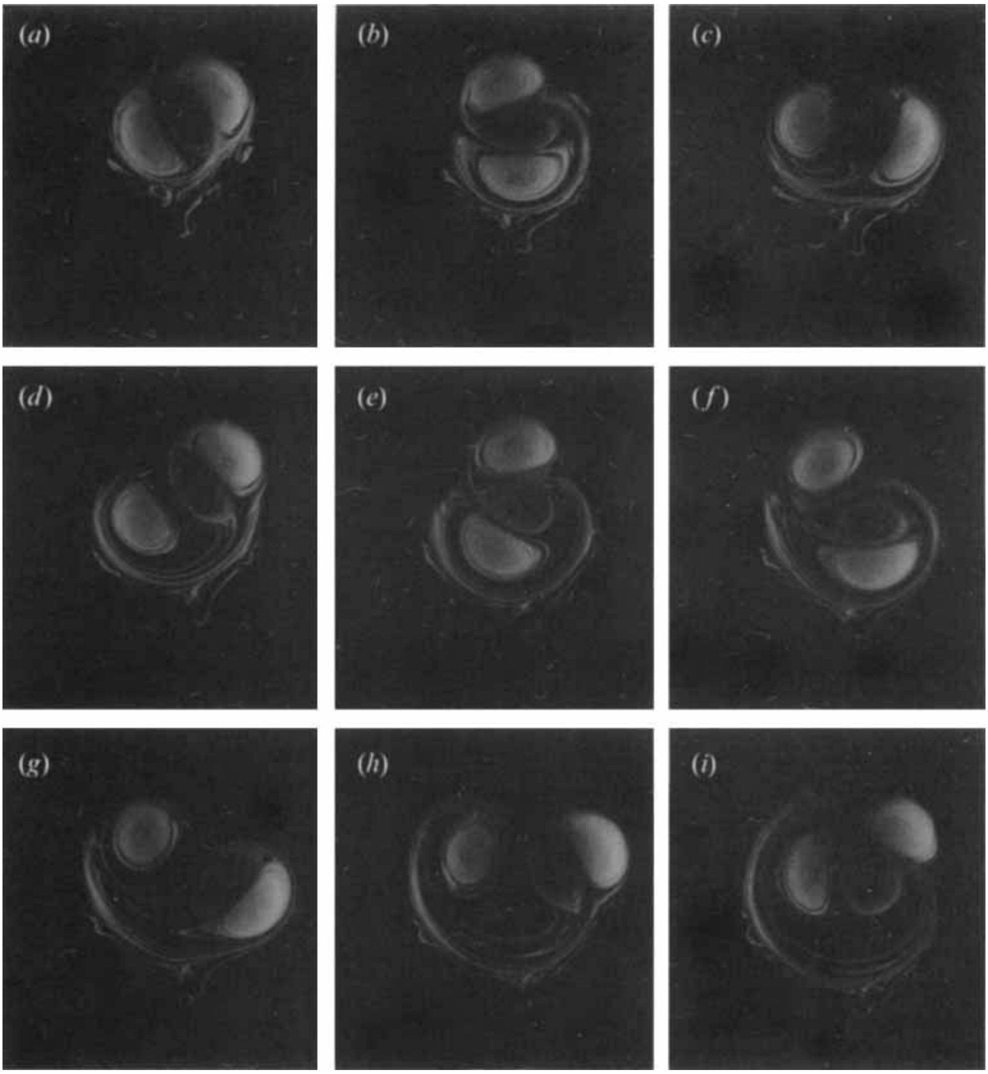

FIGURE 1. Plan-view photographs showing the evolution of a tripolar vortex in a rotating free-surface fluid (experimental parameters $h_0 = 17$ cm, $\Omega = 0.56$ s^{-1}, $R = 30$ cm). Pictures were taken at times $t = 0.9$ (*a*), $5.4T$ (*b*), $7.2T$ (*c*), $9T$ (*d*), $10.8T$ (*e*), $12.6T$ (*f*), $14.9T$ (*g*), $18.46T$ (*h*), and $22.1T$ (*i*), with the rotation period of the table $T = 11.1$ s.

in figure 1(*h*,*i*). It is clear that a patch of fluid that at some stage enters the tail, is later subjected to repeated stretching and folding. This indicates that the advection of fluid parcels is chaotic in some flow regions.

In the following sections we study in detail the motion of the vortices as well as the advection of fluid parcels. This will be done with two point-vortex models: in the first one the point vortices have constant circulations but they form initially an asymmetric tripole, whereas in the second model the point vortices form initially a symmetric tripole but their circulations are modulated (i.e. they are given by a prescribed function of space, which accounts for the squeezing and stretching of fluid columns).

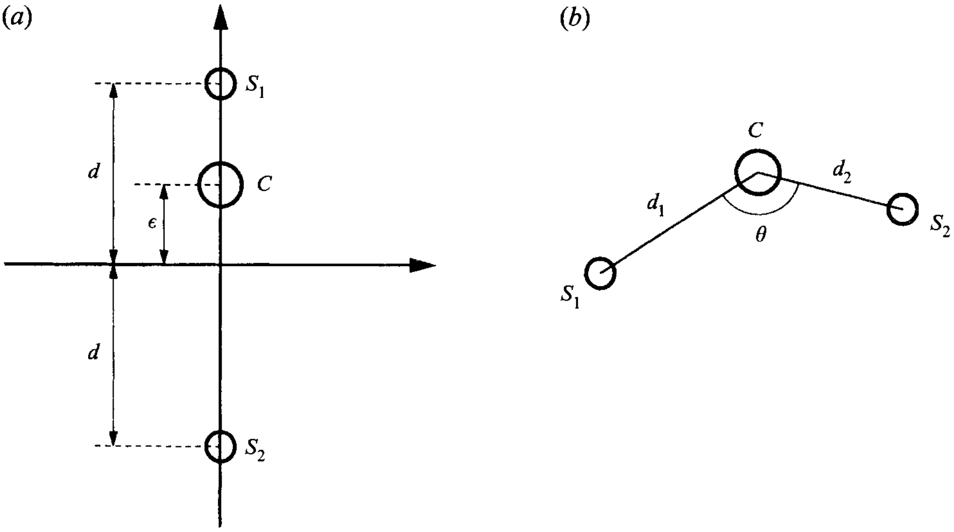

FIGURE 2. (a) Initial configuration of the point vortices in the asymmetric tripole with ϵ respresenting the asymmetry; (b) general configuration of the system: d_1 is the distance between satellite 1 (S_1) and the central vortex (C), d_2 is the distance between satellite 2 (S_2) and C, and θ is the angle between the lines joining S_1 and S_2 with C (measured in an anticlockwise sense from S_1 to S_2).

We have chosen a point-vortex representation because it models properly some features of steady tripoles with a continuously distributed vorticity (van Heijst *et al.* 1991), although this simple model cannot reproduce the generation of relative vorticity (i.e. Rossby wave radiation) that occurs in a system with non-uniform ambient vorticity. Nevertheless, Velasco Fuentes & van Heijst 1994 and Velasco Fuentes, van Heijst & Cremers 1995 found that the numerical results obtained with a modulated point-vortex model compare well with experimental observations of dipolar vortices on a (topographic) β-plane, at least for some period. Notice, incidentally, that the gradients in the ambient vorticity used by these authors are ten times larger than the ones considered in this paper.

3. Vortex motion

3.1. *A non-modulated point-vortex tripole*

Three point vortices display a large variety of regimes of motion as the vortices' strengths and relative positions are changed. It therefore cannot be a surprise that the three-vortex problem has attracted the attention of scientists for more than a century. In fact, it was already known to Poincaré (1893) that the motion of three vortices with arbitrary circulations is integrable. However, the actual reduction of the motion to quadratures has been the subject of numerous works (Gröbli 1877; Synge 1949; Novikov 1976; Aref 1979).

Our interest in the motion of three point vortices stems from observations of tripolar vortices generated in a rotating fluid. These vortices usually have zero total circulation – like the monopolar vortices from which they originate – and their two satellites possess equal circulations (van Heijst *et al.* 1991). As a consequence, the parameter set is considerably reduced: the point vortices are assumed to have the strengths $-\kappa_0, 2\kappa_0, -\kappa_0$ (with $\kappa_0 > 0$), and to be located on the y-axis at time $t = 0$ (figure 2a). The vortices with circulations $-\kappa_0$ are called satellites, the one located at

$y = d$ being denoted by S_1 and the one at $y = -d$ by S_2. The central vortex (with circulation $2\kappa_0$) is located at $y = \epsilon d$ and will be denoted by C. This choice does not represent a loss of generality, since more general initial configurations reach this particular one in the course of the motion of the vortices. Those configurations can thus be transformed into our 'reference tripole' after an appropriate rotation of the coordinate system and by a rescaling of time and length.

The motion of such a set of point vortices has been studied by Rott (1989), who showed that it can be effectively reduced to an advection problem in a two-dimensional steady field (the phase space), whereas Aref (1989) showed that this reduction is possible for all sets of three point vortices with vanishing total circulation.

The motion of a system of point vortices on an infinite domain is given by the Hamiltonian equations (see e.g. Batchelor 1967)

$$\kappa_i \frac{\mathrm{d}x_i}{\mathrm{d}t} = \frac{\partial H}{\partial y_i}, \qquad \kappa_i \frac{\mathrm{d}y_i}{\mathrm{d}t} = -\frac{\partial H}{\partial x_i}, \tag{3.1}$$

with

$$H = -\frac{1}{4\pi} \sum_{\substack{i,j=1 \\ i \neq j}}^{N} \kappa_i \kappa_j \ln r_{ij},$$

where $r_{ij}^2 = (x_i - x_j)^2 + (y_i - y_j)^2$. The first integral of motion is the Hamiltonian itself, which does not depend explicitly on time. Three more integrals can easily be obtained from invariance with respect to translation and rotation:

$$Q = \sum_{i=1}^{N} \kappa_i x_i, \qquad P = \sum_{i=1}^{N} \kappa_i y_i, \qquad I = \sum_{i=1}^{N} \kappa_i (x_i^2 + y_i^2).$$

For the configuration of three vortices defined above these conserved quantities have the following values:

$$Q_R = 0, \tag{3.2}$$

$$P_R = 2\kappa_0 \epsilon, \tag{3.3}$$

$$I_R = -2\kappa_0 (1 - \epsilon^2), \tag{3.4}$$

$$H_R = -\frac{\kappa_0^2}{2\pi} \ln \frac{2}{(1 - \epsilon^2)^2}, \tag{3.5}$$

where the subindex R indicates 'reference configuration' and lengths have been scaled by d.

In the non-modulated case the vortex circulations are constant; therefore, as the absolute positions of the vortices are not important, the distances between the vortices are sufficient to describe the *state of the system* (Aref 1979). It is more convenient, though, to choose the distance d_1 between C and S_1, the distance d_2 between C and S_2, and the angle θ between the line joining the central vortex with the satellites (figure 2*b*). This choice allows a distinction between two configurations where the point vortices are located at the vertices of similar triangles but in a different order.

In the discussion below, frequencies are scaled by the angular frequency $\Omega_0 = 3\kappa_0/4\pi d^2$ of the symmetric tripole ($\epsilon = 0$), time is scaled by the rotation period $T = 2\pi/\Omega_0$, velocities by the velocity $U = \kappa_0/4\pi d$ of a symmetric dipole, and lengths have been scaled by d.

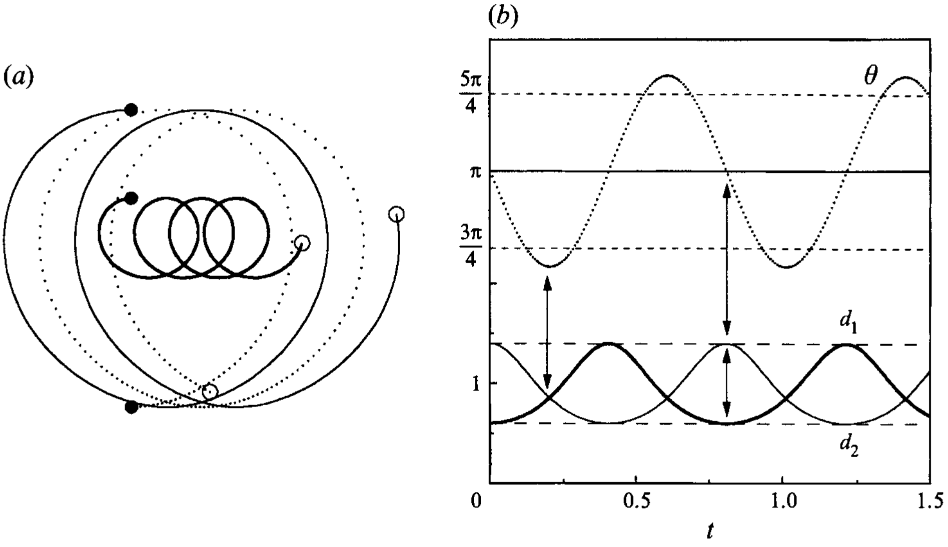

FIGURE 3. Behaviour of the asymmetric point-vortex tripole: (*a*) trajectories of the point vortices C (thick line), S_1 (thin line) and S_2 (dotted line). (*b*) Evolution of the distances d_1 and d_2 and the angle θ. The calculations were performed for $\epsilon = 0.4$.

An example of the vortex trajectories of an initially asymmetric point-vortex tripole ($\epsilon = 0.4$) is shown in figure 3(*a*), where the vortices' initial and final positions are indicated by filled and open dots, respectively. In addition to the periodic rotations of the satellites, the structure has a net translation in the positive x-direction, which is the case for all $\epsilon > 0$ (for $\epsilon < 0$ the translation occurs in the negative x-direction).

Figure 3(*b*) shows the time evolution of the distances d_1 (thick line) and d_2 (thin line), and the angle θ (dotted line). As is indicated by the two aligned arrows in figure 3(*b*), when the three vortices are aligned [$\theta(t) = \pi$] the distances $d_1(t)$ and $d_2(t)$ reach extreme values (one reaches a maximum and the other a minimum). This is so because an extreme value of the distance from a satellite to the central vortex must occur when the two vortices have zero velocity relative to each other, which happens only when all vortices are aligned or in the shape-preserving equilateral-triangle configuration – for this particular system of point vortices. Similarly, as is indicated by the single arrow in figure 3(*b*), when the vortices are located at the vertices of an isosceles triangle ($d_1 = d_2$) the angle θ reaches an extreme value (maximum or minimum). This must be so because the time derivative of θ is zero when both satellites rotate at the same rate around the central vortex, i.e. when they are located at the same distance. These two properties can be formally proved using the system's Hamiltonian function found by Rott (1989).

Rott (1989) also showed, using the same Hamiltonian function, that three regimes of motion may arise as a function of the initial asymmetry ϵ (NB Rott uses the more general definition $b = P/2\kappa_0$, which is equal to ϵ for our particular choice of initial configuration): (i) for $\epsilon \to 0$ the three vortices are separated by distances of the same order during the whole evolution; (ii) for $\epsilon \to 1$ the central vortex is close to S_1 while S_2 permanently remains at a much larger distance; and (iii) for $\epsilon \gg 1$ the two satellites are close together while the central vortex remains far from them. We consider here how the frequency, the mean speed and the perturbation amplitude of d_1, d_2 and θ vary in the range $0 < \epsilon < 1$, i.e. only in the first two regimes of motion. The critical

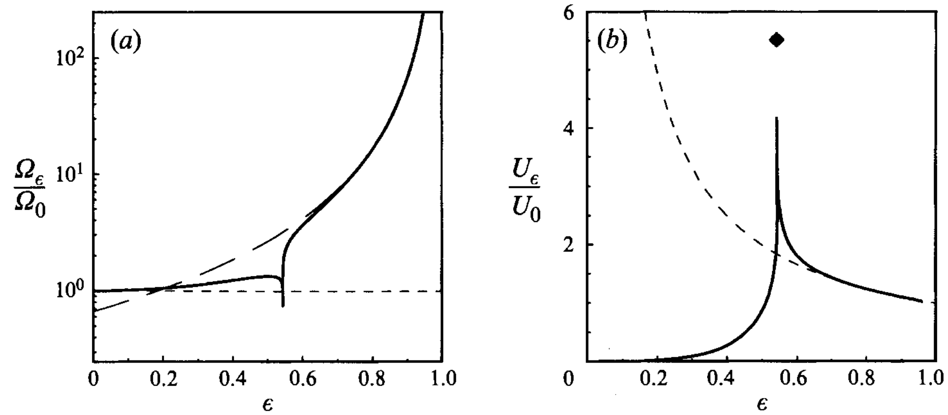

FIGURE 4. (*a*) Frequency Ω_ϵ and (*b*) mean propagation speed U_ϵ of the tripole configuration shown in figure 2(*a*) as a function of the initial perturbation ϵ of the position of C. These quantities are scaled by the frequency $\Omega_0 = 3\kappa_0/4\pi d^2$ of the symmetric tripole ($\epsilon = 0$), and the velocity $U = \kappa_0/4\pi d$ of the symmetric dipole ($\epsilon = 1$).

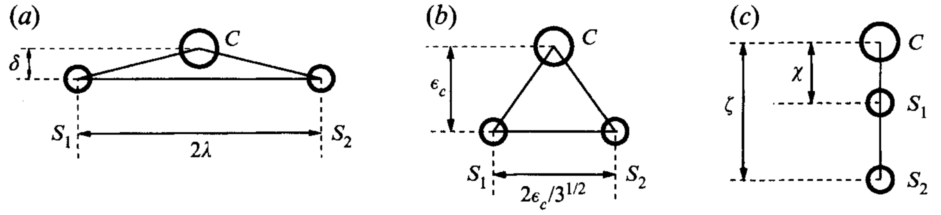

FIGURE 5. Intermediate stages for different regimes of motion. (*a*) *Tripole regime*: at time $t = T/4$ the vortices form an isosceles-triangle configuration; at this point C pairs with S_2, leaving S_1 behind. (*b*) For the critical value $\epsilon_c \approx 0.544$ the vortices move asymptotically towards an equilateral-triangle configuration which translates steadily. (*c*) *Dipole–monopole regime*: for $\epsilon > 0.544$ the three vortices reach a new linear configuration at $t = T/2$, but now C occupies an extreme position. T is the period of the motion.

value ϵ_c at which the change from regime (i) to regime (ii) takes place is also briefly discussed.

Tripole regime

The tripole regime occurs in the range $0 < \epsilon < \epsilon_c$. For all $\epsilon \neq 0$ vortices C and S_1 move initially in the same direction. These can be considered as forming a 'couple', with S_1 rotating around C relatively fast in comparison with the rotation of vortex S_2. Owing to its asymmetry, the couple C-S_1 moves towards S_2, and an exchange of partner takes place. The new couple C-S_2 moves initially away from S_1, but it is also asymmetric and moves back to re-encounter S_1. A periodic motion, with C pairing in turn with S_1 and S_2, arises. The angular frequency Ω_ϵ of this motion increases slightly from 1, and reaches its maximum value at $\epsilon \approx 0.49$, see figure 4(*a*). A further increase of ϵ leads to a large decrease of the frequency. The tripole's mean translational speed increases continuously from zero at $\epsilon = 0$. For small ϵ the increase is slow and it is faster as ϵ approaches its critical value (figure 4*b*).

In this regime the vortices reach an isosceles-triangle configuration after one quarter of a period (figure 5*a*). Vortices S_1 and S_2 are located at the ends of the triangle's base, which has a length of 2λ. Vortex C is located at (x, y), at a distance δ from the base of the triangle. The integrals of motion uniquely determine the size and shape of the configuration and the value of the coordinate y, whereas x remains undetermined. The integrals of motion are given at this stage by

$$\begin{aligned} P_I &= 2\kappa_0\delta, \\ I_I &= -2\kappa_0(\lambda^2 - 2\delta y + \delta^2), \\ H_I &= -\frac{\kappa_0^2}{2\pi}\ln\frac{2\lambda}{(\delta^2+\lambda^2)^2}, \end{aligned}$$

where the subindex I indicates 'isosceles-triangle configuration'. Conservation of P, I and H during the whole evolution implies that

$$\delta = \epsilon, \tag{3.6}$$

$$y = \frac{\lambda^2 + 2\epsilon - 1}{2\epsilon}, \tag{3.7}$$

$$(\lambda^2 + \epsilon^2)^2 - (1-\epsilon^2)^2\lambda = 0, \tag{3.8}$$

The height of the triangle is thus equal to ϵ and the length 2λ of its base can be obtained from the third equation. Once λ is known, the position y of the central vortex follows from the second equation.

Dipole–monopole regime

Beyond the critical point ($\epsilon_c < \epsilon < 1$), one finds the dipole–monopole regime. C and S_1 can be considered as being a couple since the distance between them is much smaller than that between C and S_2. The couple thus rotates owing to its own asymmetry and propagates owing to the presence of the third vortex (S_2), which in turn shows an average translation with a wobbling perturbation superimposed. The frequency in this range is again a growing function of ϵ (thick line in figure 4*a*). An empirical approximation of it is given by the rotation frequency of an asymmetric dipole formed by vortices C and S_1 (assuming that S_2 has no influence on this couple). The angular frequency of this asymmetric dipole is given (in dimensional form) by $\Omega_D = \kappa_0/2\pi d^2(1-\epsilon)^2$, which approximates well the frequency of the three-vortex system for $\epsilon \to 1$ (the broken line in figure 4*a*).

The mean translation speed U_ϵ of the three vortices decreases with growing ϵ (thick line in figure 4*b*). An empirical approximation for this speed is obtained by defining a *virtual dipole*, which is formed by vortex S_2 and a vortex with the same total circulation as the asymmetric couple C-S_1 located at the centre of rotation of this couple. The virtual dipole so defined moves with a (dimensional) velocity given by $U_D = \kappa_0/4\pi\epsilon d$ (represented by the broken line in figure 4*b*). This velocity is a good approximation of the mean velocity of the three vortices as $\epsilon \to 1$.

Since the central vortex C does not change partner in this regime, the vortices never reach an isosceles-triangle configuration. Instead, they take positions on a straight line after one half-period (figure 5*c*), but now the central vortex C occupies an extreme position in the linear configuration. Satellite S_1 is separated by a distance χ from C, and S_2 by a distance ζ. As before, the integrals of motion may be used to determine the values of χ and ζ as functions of the initial perturbation ϵ.

Equilateral triangle

At the critical value ϵ_c, the initial linear configuration transforms asymptotically into an equilateral triangle with sides $2(3)^{-1/2}\epsilon_c$ (see figure 5*b*). The critical value can be found by substituting $\epsilon = \epsilon_c$ and $\lambda = (3)^{-1/2}\epsilon_c$ in (3.8) and solving numerically for ϵ_c, which yields $\epsilon_c \approx 0.543997$.

The triangular configuration translates, without change of size or shape, at a constant speed $U_c = 3\kappa_0/4\pi\epsilon d$ (indicated by a diamond in figure 4*b*). This configuration is unstable, i.e. it corresponds to a fixed point of hyperbolic type in the phase space (Rott 1989). Since it takes an infinite time to reach a hyperbolic fixed point (or to escape from it) the frequency of the system is zero. The frequency is larger than zero (and the velocity smaller than U_c) in figure 4 because calculations have been done close to, but not at, the critical point.

The asymmetric configuration discussed in this section reproduces some of the features observed in the experiments. In particular, it renders the essentially time-dependent behaviour of the tripole, which goes in succession through linear and isosceles-triangle configurations. However, it fails to reproduce the growing amplitude of the asymmetry, which is in fact approximately zero as the tripole is formed. In other words, this model describes the evolution of an asymmetric tripole, but it does not explain how the asymmetry arises. The following section is intended to provide an answer to the latter issue.

3.2. *A modulated point-vortex tripole*

Laboratory experiments like the one discussed in §2 have shown that the evolution of the tripole is strongly influenced by its initial separation from the axis of rotation. This suggests that the unsteadiness of the tripole is caused by the parabolic free surface of the rotating fluid in which the vortex is generated. As the satellites rotate around the central vortex the non-uniformity of the fluid depth produces a continuous stretching and squeezing of fluid columns, which, having to preserve potential vorticity, alternately gain and lose relative vorticity. These effects can be incorporated in the point-vortex model by assuming that each point vortex represents a small patch of vorticity (see e.g. Kono & Yamagata 1977; Zabusky & McWilliams 1982). The circulation κ_i therefore equals the (uniform) vorticity $\bar{\omega}_i$ multiplied by the area of the patch a_i. Conservation of potential vorticity implies that the relative vorticity ω of a fluid patch moving in the latitudinal direction changes as expressed by (2.2) or (2.3). These equations, in addition to area conservation, yield the modulation equation for the vortex circulation (see e.g. Velasco Fuentes 1994)

$$\kappa_i = \kappa_{i0} - \gamma_*(r_{i0}^2 - r_i^2), \tag{3.9}$$

where $\gamma_* = \pi L^2 \gamma$ (with L the radius of the area associated with the 'point' vortex), and r_{i0} is the distance from the tank centre to the point vortex' initial position, at which the vortex has strength κ_{i0}.

We study the evolution of the point-vortex tripole on the γ-plane as a function of two parameters: (*a*) γ_*, which represents the curvature of the free surface; and (*b*) the initial position of the tripole, expressed by the distance R of the central vortex from the rotation axis or pole. Initially the vortices are located on a straight line and the satellites are separated by the same distance d from C (figure 6*a*). In all cases discussed here the linear arrangement is tangent to the circle $r = R$ at the position of C (figure 6*a*).

Owing to their modulated strengths, the motion of the point vortices is essentially determined by their absolute positions. The three coordinates used in the previous

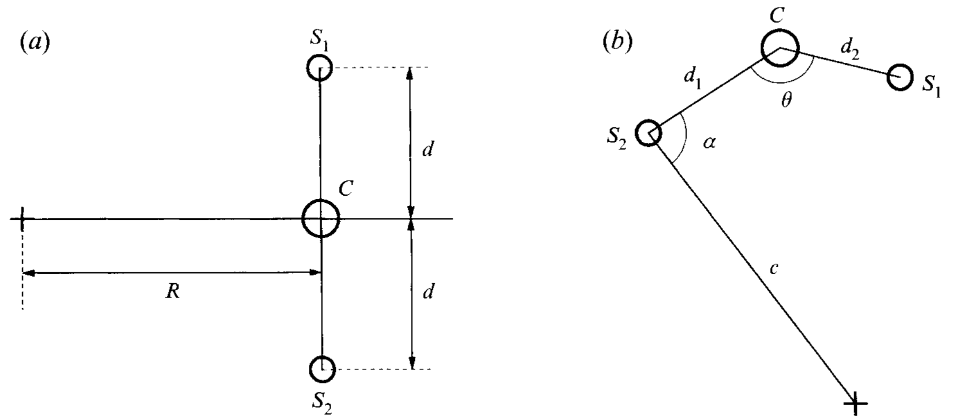

FIGURE 6. (*a*) Initial conditions of a symmetric point-vortex tripole on a γ-plane. (*b*) General configuration of three point vortices on a γ-plane. The parameters d_1, d_2 and θ are defined as in figure 2(*b*), c is the distance from S_2 to the pole and α is the angle between the lines joining S_2 to the pole and to C.

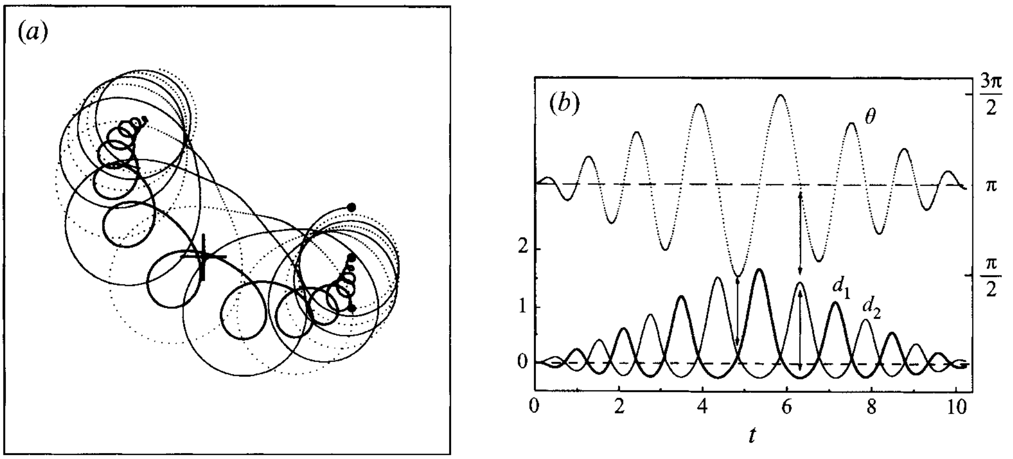

FIGURE 7. Modulated point-vortex tripole on the γ-plane: (*a*) typical trajectories of the individual vortices C (thick line), S_1 (thin line) and S_2 (dotted line); (*b*) evolution of the parameters d_1, d_2 and θ. The calculations were performed for $\gamma_* = 0.01$ and $R = 3$.

section are thus not enough to uniquely describe the state of this system. Although six coordinates are needed to determine the absolute positions of three points in a plane, the rotational symmetry of the parabolic free surface (or the γ-plane) reduces to five the number of coordinates that uniquely determine the state of the system. These are chosen to be the distances d_1 and d_2 and the angle θ, which define the relative positions of the vortices, in addition to the distance c from the centre to vortex S_2 and the angle α between this line and the line joining S_2 and C (figure 6*b*).

The point-vortex tripole typically evolves as follows (see figure 7*a*). As the satellites rotate around C, S_1 moves towards shallower regions and thus becomes stronger (more negative) while S_2 moves towards deeper areas and becomes weaker (less negative). As a consequence, the velocities induced by the satellites on the central vortex do not cancel each other anymore and C begins to move in the direction of the stronger satellite (S_1). Although initially small, this asymmetry is enough to induce a

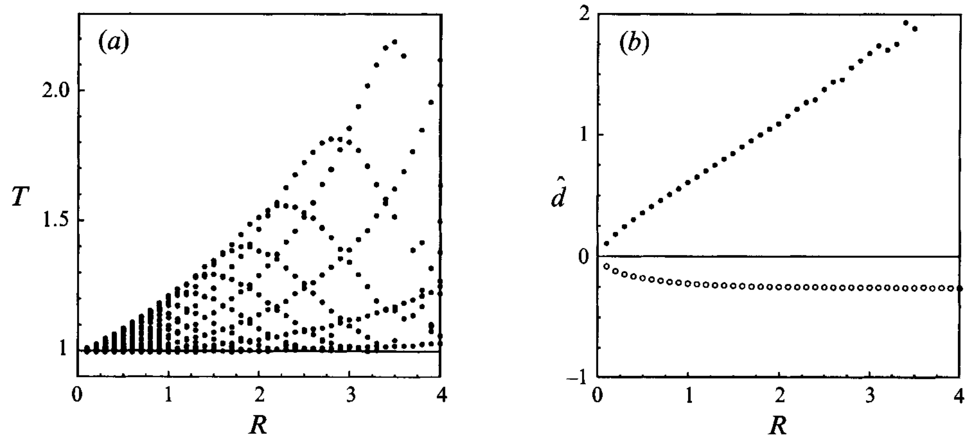

FIGURE 8. (*a*) Rotation periods during one excursion of the modulated point-vortex tripole on the γ-plane and (*b*) $\hat{d}_{max}$ (filled dots) and $\hat{d}_{min}$ (open dots), as a function of the initial position (R) of the tripole (and for a constant $\gamma_* = 0.01$). The solid lines give the corresponding values for the unperturbed tripole.

net centreward drift to the tripole. This shift increases the asymmetry, which in turn strengthens the tripole's drift, as has been shown in §3.1 for the non-modulated case. However, because the isobaths are circles and the drift is not straight centrewards, the tripole reaches a maximum centreward displacement and continues its drift but now away from the centre. The asymmetries decrease and the tripole approximately reaches the initial symmetric state as it returns to its initial radial position.

The evolution of each of the parameters d_1, d_2 and θ also illustrates this behaviour (figure 7*b*). Two characteristic periods can be defined in these time series: (i) the *rotation period* is the time it takes for the satellites to rotate around C and is computed as the time between two adjacent local extreme values of d_1; and (ii) the *excursion period* is the time it takes for the tripole to move towards the centre and back to its initial radial position (e.g. figure 7*a* shows vortex trajectories during one complete excursion).

The rotation periods displayed by the tripole for different initial positions are shown in figure 8(*a*). Each dot represents one rotation of the satellites and all dots lying on the same vertical line originate from the same simulation. For example, in the numerical experiment shown in figure 7(*a*) S_1 and S_2 rotate approximately eight times around C: there are thus eight points on the vertical line $R = 3$ in figure 8(*a*). It is obvious that for all initial conditions the first rotations of the satellites around C are completed in a period approximately equal to that of the unperturbed tripole (represented by the solid line). However, the rotation period becomes longer as the tripole moves towards the centre. This feature originates from the larger distance between the satellites and the central vortex, in addition to the lower strength of C and higher strengths of S_1 and S_2. Therefore, as the initial position R increases, the range of values of the rotation period also grows, with the lower limit remaining approximately constant and the higher one increasing.

In addition, figure 8(*b*) shows the extreme values of the perturbation of the distance $d_1(t)$ as a function of the initial position R. The filled circles represent $\hat{d}_{max} = \max(d_1) - 1$ and the open circles $\hat{d}_{min} = \min(d_1) - 1$, where max (d_1) and min (d_1) are the maximum and minimum values of $d_1(t)$ during one excursion of the

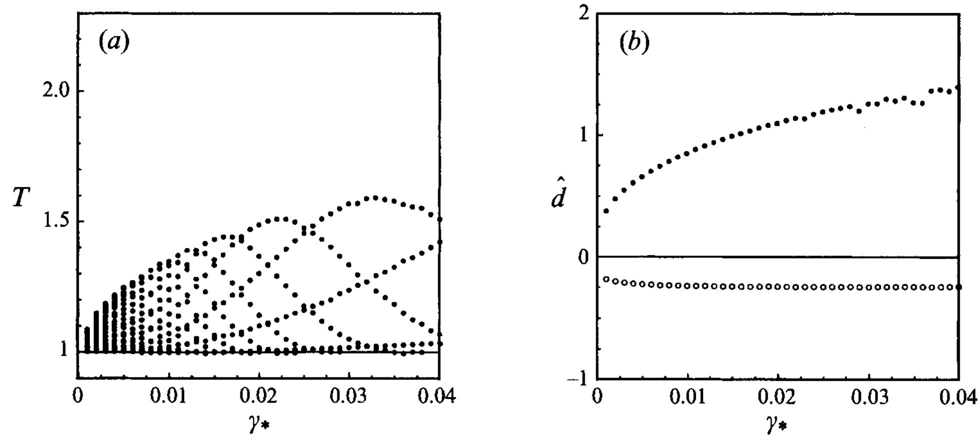

FIGURE 9. The same as in figure 8, but now as a function of γ_* and for constant distance to the centre $R = 1.5$.

tripole, respectively. The graph shows that $\hat{d}_{max}$ grows linearly as R increases, whereas $\hat{d}_{min}$ smoothly decreases as R becomes non-zero and remains approximately constant with further growth of R (in the range of values considered here).

Similar effects are observed if the initial position of the tripole is kept constant and the value of γ_* is varied. For $\gamma_* = 0$ the unperturbed symmetric tripole is recovered, and with increasing γ_* the range of values of the rotation period broadens (figure 9*a*). The broadening occurs towards longer periods, as is the case for increasing initial distance to the centre. The value of $\hat{d}_{max}$ grows in a nonlinear manner with γ_* (see figure 9*b*), whereas $\hat{d}_{min}$ is approximately constant – but smaller than the unperturbed value – for the range of parameters studied here.

Some remarks about the integrability of the motion of a modulated point-vortex tripole are in order. If the numerical experiments are allowed to continue for several excursions of the tripole then more rotation periods appear, although all of them lie within the same range displayed during the first excursion (e.g. figures 8*a* and 9*a*). Furthermore, it is observed that the set of vortices stays within the tripole regime defined in §3.1. This result suggests that the motion of the modulated tripole is integrable in the parameter region explored in this paper ($0 < R < 4$ and $0 < \gamma_* < 0.04$). However, for larger values of R the three point vortices have been observed to enter the dipole–monopole regime and then go back to the tripole regime, i.e. at least one linear-configuration event occurred with C *not* located between the satellites. An analogy with the advection of a passive scalar suggests that these regime changes might be an indication of chaotic behaviour of the system. Indeed, passive scalars can have chaotic trajectories when they enter and leave regions of qualitatively different motions in the course of the flow evolution (see e.g. §4.1 below).

3.3. *Comparison of experimental and numerical results*

The trajectory described by each vortex in the laboratory experiment discussed in §2 is displayed in figure 10(*a*). The thick line represents the path of the central vortex, the thin line that of S_1, and the dotted line that of S_2. Two features are clearly seen in this figure: (i) the increasing amplitude of the cycloid-like motion of the central vortex; and (ii) the westward drift of the structure as a whole (the cross indicates the tank's centre, which is the pole of the topographic γ-plane). Both effects can also be seen in the evolution of the parameters d_1, d_2, and θ (figure 11*a*). In this figure

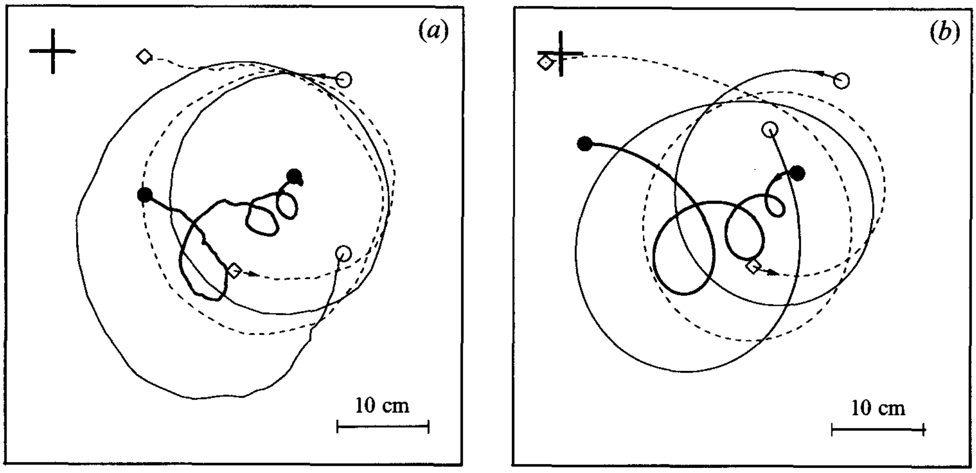

FIGURE 10. (*a*) Observed trajectories of the vortex centres of the tripolar vortex shown in figure 1 and (*b*) numerical simulation of (*a*) using three modulated point vortices. The central vortex C is represented by a thick line, S_1 by a thin line and S_2 by a dotted line.

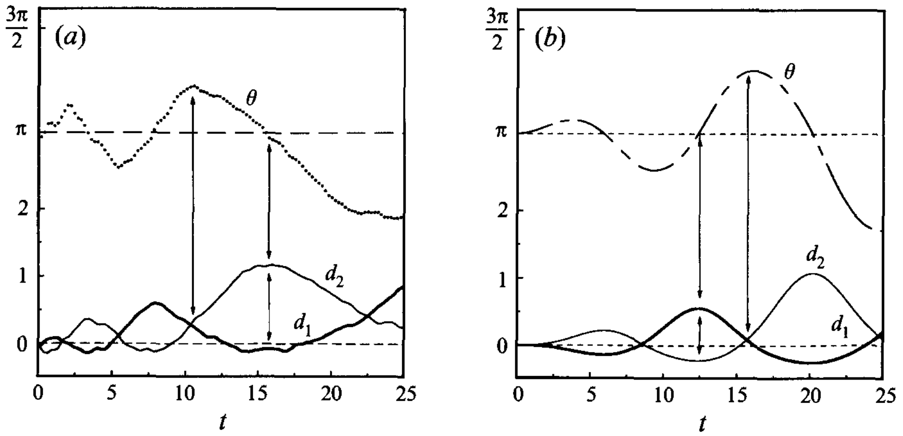

FIGURE 11. Evolution of the parameters $d_1(t)$, $d_2(t)$ and $\theta(t)$ for: (*a*) the laboratory experiment shown in figure 10(*a*); and (*b*) the numerical simulation shown in figure 10(*b*).

the two aligned arrows indicate that extreme values of d_1 and d_2 occur at a linear configuration ($\theta = \pi$), whereas the single arrow indicates that an isosceles-triangle configuration ($d_1 = d_2$) is reached when the angle θ takes a local extreme value, as in the point-vortex models described in previous sections.

A numerical simulation was performed to compare with these experimental observations. The value of γ and the initial positions of the point vortices were chosen to correspond to those of the experimental situation, and the radius of the circular area assigned to the point vortices was taken as $d/2$, where $d = 11$ cm is the initial distance from the satellites to the central vortex.

The circulations of the point vortices in the model $(-\kappa_0, 2\kappa_0, -\kappa_0)$ were then estimated by considering the rotation of a symmetric point-vortex tripole. This rotation has an angular speed given by $\Omega_t = 3\kappa_0/4\pi d^2$, where Ω_t is the tripole's angular speed in the experiment. The decay is taken into account by using a mean angular speed

$$\Omega_t = \frac{1}{\tau}\int_0^\tau \Omega_{max} e^{-\alpha t} dt,$$

where Ω_{max} is the measured initial angular speed (0.33 s^{-1}), τ is the duration of the experiment (300 s), and the value of α (0.013 s^{-1}) was computed using the results of van Heijst *et al.* (1991), who measured an exponential decay of the angular speed of the steady tripolar vortices. This decay is most likely due to the bottom Ekman layer.

As observed in the experiment, the resulting vortex trajectories (figure 10*b*) show growing cycloids and the structure drifts towards the centre along a curved path. Figure 11(*b*) shows the evolution of the parameters d_1, d_2 and θ in this simulation, which shows a good agreement with the observations (figure 11*a*), as can be expected from the good agreement between the observed and the computed vortex trajectories. However, owing to the discrete representation of the continuous distribution of vorticity, the numerical series are smoother than the experimental ones. There is also a time shift between these time series: the numerical tripole evolves more slowly. This is probably due to the use of a large α for the Ekman decay of the angular speed, which was chosen as an average of the values measured by van Heijst *et al.* (1991).

4. Advection by an unsteady tripole

The complicated dye patterns observed in figure 1 are the result of the essentially time-dependent motion of the tripole. This behaviour is also displayed in the two models described in §§ 3.1 and 3.2, namely: (i) an asymmetric linear arrangement without modulation; (ii) an initially symmetric tripole with modulation.

The non-modulated point-vortex tripole displays a periodic motion and this may lead to chaotic particle trajectories, as for any unsteady two-dimensional velocity field (see e.g. Aref 1984). Moreover, the motion is periodic, in which case we do not need to study the particle trajectories continuously in time: it is sufficient to know their positions every time the tripole returns to a reference configuration. This stroboscopic description (known as a Poincaré map in the theory of dynamical systems) greatly simplifies the analysis of particle motion. The techniques used in this analysis are discussed in detail by e.g. Rom-Kedar, Leonard & Wiggins (1990) and Wiggins (1992), whereas applications of these techniques in problems similar to the one discussed here can be found in e.g. Velasco Fuentes (1994) and Velasco Fuentes *et al.* (1995).

Although the non-modulated model does not reproduce the growing asymmetry observed in the laboratory situation, we believe that a good understanding of particle advection in this model helps in addressing the more complicated particle motion that arises in the modulated point-vortex tripole. For this reason, we will first discuss the transport characteristics of the non-modulated tripole model, before considering the effects of the modulation.

4.1. *Advection by an asymmetric point-vortex tripole*

The motion of fluid particles in the velocity field of an asymmetric tripole is most conveniently described by choosing a reference system in which the point vortices are either at rest or move periodically around an unperturbed position. The choice made here is a system that moves with the time-dependent velocity $\boldsymbol{u}(t)$ of the central vortex C, and rotates with the average angular velocity Ω_ϵ of the satellites around C. It will

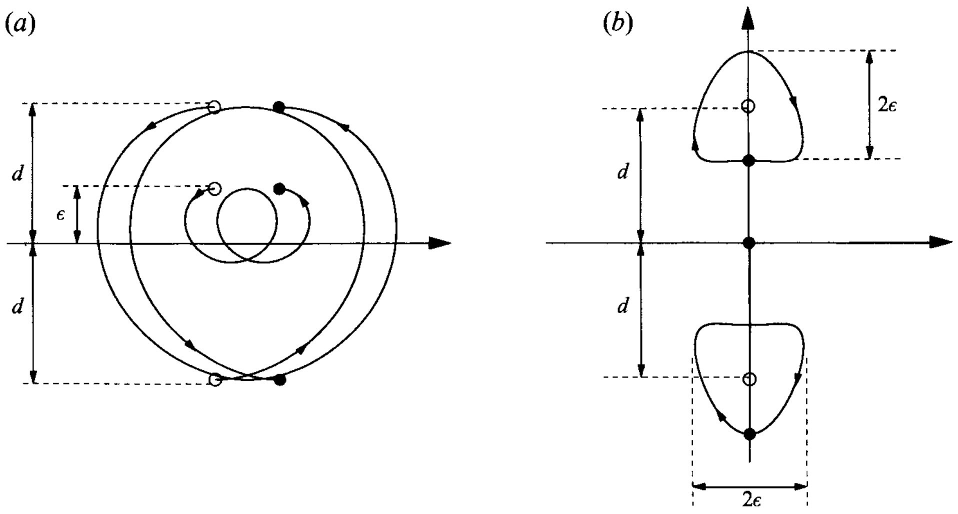

FIGURE 12. (*a*) Trajectories of the point vortices in a frame fixed in space (ϵ=0.4); (*b*) the same trajectories in a frame moving with the central vortex and rotating with the frequency of the satellites (see text).

prove convenient to write the velocity and the angular speed in the following way:

$$\boldsymbol{u} = (\epsilon U', \epsilon V'), \tag{4.1}$$

$$\Omega_\epsilon = \Omega_0 + \epsilon \Omega', \tag{4.2}$$

where ϵ is the initial shift of the central vortex C, and Ω_0 is the angular speed of the symmetric tripole. In these equations the primed variables are essentially time dependent, and the factor ϵ stresses the fact that they appear only if the structure is asymmetric ($\epsilon \neq 0$). Note that Ω_ϵ is given (in non-dimensional form) in figure 4(*a*), whereas the velocity U_ϵ given in figure 4(*b*) is the average value of U' over one period of the tripole's motion. Figure 12(*a*) shows the trajectories of the point vortices in a frame fixed in space for the case $\epsilon = 0.4$, while the same trajectories in the co-moving frame are shown in figure 12(*b*). In this moving system the satellites rotate around the unperturbed position $(0, \pm d)$ in a clockwise sense.

The equations of motion of a fluid particle in the moving frame are given by

$$\frac{\mathrm{d}x}{\mathrm{d}t} = \frac{\kappa_0}{2\pi}\left(\frac{Y_1}{I_1} + \frac{Y_2}{I_2} - \frac{2y}{I_0}\right) + (\Omega_0 + \epsilon\Omega')y - \epsilon U', \tag{4.3}$$

$$\frac{\mathrm{d}y}{\mathrm{d}t} = -\frac{\kappa_0}{2\pi}\left(\frac{X_1}{I_1} + \frac{X_2}{I_2} - \frac{2x}{I_0}\right) - (\Omega_0 + \epsilon\Omega')x - \epsilon V', \tag{4.4}$$

where the definitions $X_i = x - x_i$, $Y_i = y - y_i$ and $I_i = X_i^2 + Y_i^2$ have been used. The positions of the vortices are given by (x_i, y_i), with $i = 0$ for the central vortex and $i = 1, 2$ for satellites S_1 and S_2, respectively.

These equations, together with the evolution equations (3.1), govern the motion of particles in the velocity field of an asymmetric tripole. This form of the equations is suitable for most of the calculations; however, for the computation of the Melnikov function in §4.1.1 the equations must be written in the form of a periodically perturbed integrable Hamiltonian system

$$\mathrm{d}x/\mathrm{d}t = f_1(x, y) + \epsilon g_1[x, y, \boldsymbol{x}_1(t;\epsilon), \boldsymbol{x}_2(t;\epsilon)], \tag{4.5}$$

$$\mathrm{d}y/\mathrm{d}t = f_2(x,y) + \epsilon g_2[x, y, \boldsymbol{x}_1(t;\epsilon), \boldsymbol{x}_2(t;\epsilon)], \tag{4.6}$$

where $\boldsymbol{x}_i = (x_i, y_i)$ is the position of satellite i, which can be written in the following form:

$$x_i = \epsilon\xi_i, \tag{4.7}$$

$$y_1 = d + \epsilon\eta_1, \tag{4.8}$$

$$y_2 = -d - \epsilon\eta_2. \tag{4.9}$$

The perturbed form (4.5) and (4.6) is obtained by substituting (4.7)–(4.9) in (4.3) and (4.4) and expanding these equations in a Taylor series around $\epsilon = 0$. The zeroth- and first-order terms give the functions f_i and g_i:

$$f_1 = \frac{\kappa_0}{2\pi}\left(\frac{Y_-}{I_-} + \frac{Y_+}{I_+} - \frac{2y}{I_0}\right) + \Omega_0 y, \tag{4.10}$$

$$f_2 = -\frac{\kappa_0 x}{2\pi}\left(\frac{1}{I_-} + \frac{1}{I_+} - \frac{2}{I_0}\right) - \Omega_0 x, \tag{4.11}$$

$$g_1 = \frac{-I_-\eta_1 + 2Y_-(x\xi_1 + Y_-\eta_1)}{I_-^2} + \frac{I_+\eta_2 + 2Y_+(x\xi_2 - Y_+\eta_2)}{I_+^2} + \Omega' y - U', \tag{4.12}$$

$$g_2 = \frac{I_-\xi_1 - 2x(x\xi_1 + Y_-\eta_1)}{I_-^2} + \frac{I_+\xi_2 - 2x(x\xi_2 - Y_+\eta_2)}{I_+^2} - \Omega' x - V', \tag{4.13}$$

where the new definitions $Y_\pm = y \pm d$ and $I_\pm = x^2 + Y_\pm^2$ have been introduced, and I_0 is defined as before.

4.1.1. *Lobe dynamics*

In this time-periodic case a significant simplification of the description of particle motion is achieved by using the Poincaré map – the map of the particle location $[x(t_0), y(t_0)]$ to the location one period later $[x(t_0+T), y(t_0+T)]$. Loosely speaking this corresponds to sampling the position of a particle every time the tripole returns to its initial configuration (i.e. $\theta = \pi$, $a = d - \epsilon$ and $b = d + \epsilon$).

The streamline patterns of the stationary tripole ($\epsilon = 0$) are illustrated in figure 13(*a*). Four flow regions can be distinguished: the positive core, where particles rotate anticlockwise around the central vortex; two negative cores, where particles rotate clockwise around one of the satellite vortices; and the free flow region, where particles rotate clockwise around the set of vortices. The flow regions are separated by streamlines that intersect at two stagnation points. In the theory of dynamical systems these streamlines are called separatrices, whereas the point-vortex positions and the stagnation points are called fixed points of elliptical and hyperbolic type, respectively.

The lower separatrix in figure 13(*a*) is formed by a collection of *orbits* (particle trajectories) that approach the hyperbolic point p_- as $t \to +\infty$, called the *stable manifold* of p_-, and a collection of orbits that emanate from the hyperbolic point p_+ (i.e. approach p_+ as $t \to -\infty$), called the *unstable manifold* of p_+. Similarly, the upper separatrix is formed by the stable manifold of p_+ and the unstable manifold of p_-.

For $\epsilon \neq 0$, but sufficiently small, the fixed points persist and the unstable manifold of p_+ smoothly emanates from p_+ as before, but in this case undergoes strong oscillations as it approaches p_-. Similarly, but for $t \to -\infty$, the stable manifold smoothly emanates from p_- and undergoes strong oscillations as it approaches p_+. The structure that results from the intersection of the manifolds of the two hyperbolic

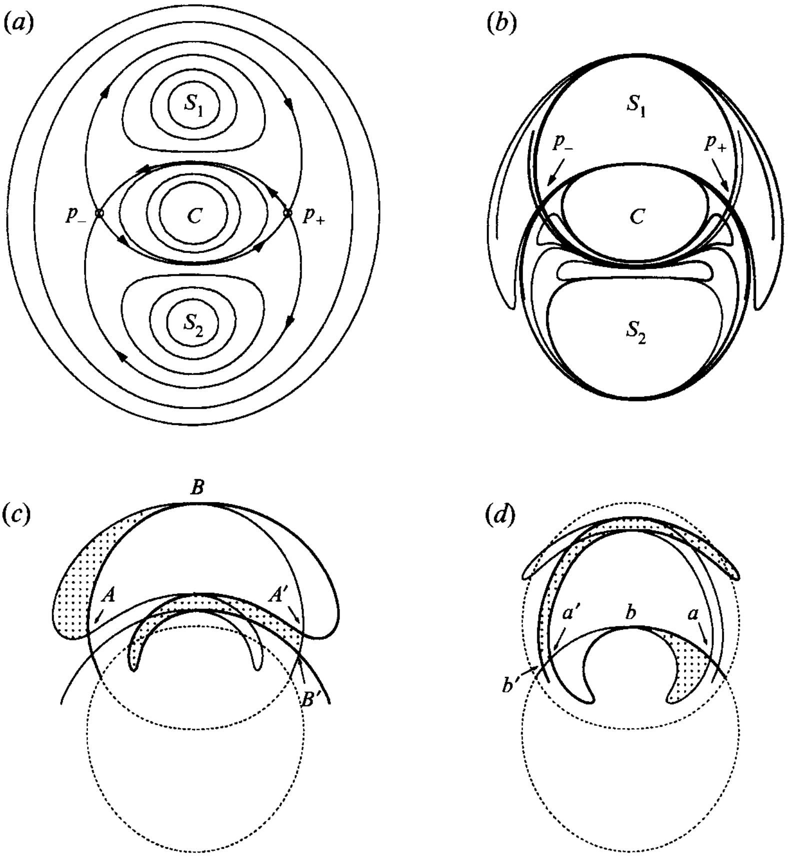

FIGURE 13. (*a*) Stream function of the unperturbed point-vortex tripole in a frame rotating with the structure; (*b*) heteroclinic tangles of the perturbed tripole; (*c*) fluid exchanged between S_1 and the ambient flow region; and (*d*) fluid exchanged between S_1 and C.

points is called a *heteroclinic tangle* (figure 13*b*), and indicates how transport of fluid between different flow regions occurs. Points A and B in figure 13(*c*), which are two adjacent intersections between the stable and unstable manifolds, are mapped to points A' and B'. Correspondingly, the dotted area close to B in figure 13(*c*) maps to the dotted area close to B'. If the boundary between the fluid trapped by satellite S_1 and the ambient fluid is redefined as p_+B along the stable manifold and Bp_- along the unstable manifold, then the area bounded by segments of the stable and unstable manifolds between A and B represents the fluid that will be entrained into S_1 in the next cycle. Since the flow is incompressible, an equal area is detrained in the same period. Similarly, the tangle formed by the stable manifold of p_- and the unstable manifold of p_+ gives rise to transport of fluid between S_1 and the central vortex C (figure 13*d*).

The unstable manifold is constructed numerically in the following way. A line with length δd, where $2d$ is the distance between the satellites and $\delta \ll 1$, is located on the fixed point and its evolution in the perturbed velocity field is computed forward in time. The line will be stretched in the direction of the unstable manifold. The stable manifold is constructed in a similar way, but the integration is now backwards in time. The exchange of mass can be evaluated directly from the discrete set of points defining the manifolds. Once a single lobe is identified the area follows from $\mu = \oint x \mathrm{d}y$

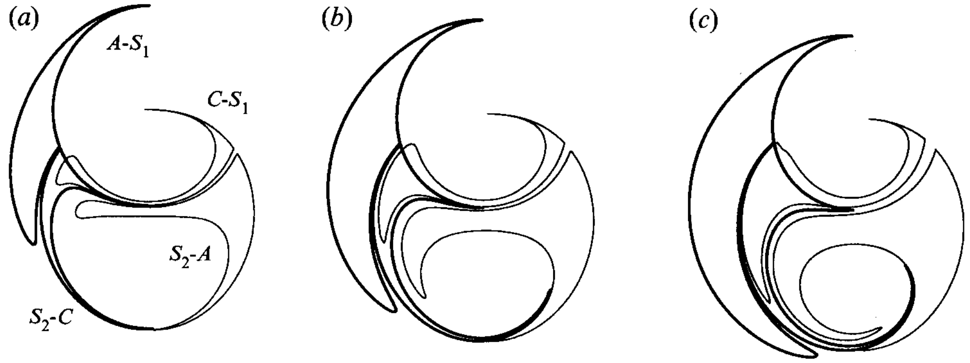

FIGURE 14. Entrainment and detrainment lobes of the perturbed point-vortex tripole for different asymmetries: (*a*) $\epsilon = 0.1$; (*b*) 0.2; and (*c*) 0.3.

along the boundary of the lobe (e.g. the segments AB on the stable manifold and BA on the unstable manifold in figure 13*c*). This method is valid for every amplitude of perturbation ϵ.

Melnikov function

The *Melnikov function* makes it possible to predict the behaviour of the stable and the unstable manifolds without explicitly solving the advection equations (4.3)–(4.4). The Melnikov function $M(t_0)$ is defined as (see e.g. Wiggins 1992)

$$M(t_0) = \int_{-\infty}^{\infty} \{f_1[\mathbf{x}_u(t)]g_2[\mathbf{x}_u(t), \mathbf{x}_1(t+t_0;\epsilon), \mathbf{x}_2(t+t_0;\epsilon)] \\ -f_2[\mathbf{x}_u(t)]g_1[\mathbf{x}_u(t), \mathbf{x}_1(t+t_0;\epsilon), \mathbf{x}_2(t+t_0;\epsilon)]\}\mathrm{d}t, \tag{4.1}$$

where $\mathbf{x}_u(t) = [x_u(t), y_u(t)]$ is the particle trajectory along the separatrix of the unperturbed tripole. Since $M(t_0)$ is a first-order approximation of the distance between the stable and unstable manifolds, one can obtain an $O(\epsilon)$ approximation for the area of a lobe by integrating this function (Rom-Kedar *et al.* 1990):

$$\mu = \epsilon \int_{t_{01}}^{t_{02}} M(t_0)\mathrm{d}t_0 + O(\epsilon^2), \tag{4.2}$$

where t_{01} and t_{02} are two adjacent zeros of the Melnikov function $M(t_0)$, i.e. they correspond to adjacent intersections of the unstable and stable manifolds.

4.1.2. *Numerical results*

Figure 14 shows some of the lobes that will be detrained or entrained during the next period for different values of the perturbation ϵ. The thick lines represent entrainment lobes of satellite 1 and the central vortex, while the thin lines represent detrainment lobes of the central vortex and satellite 2. The letters in figure 14(*a*) indicate the region where the lobes are located at times $t = nT$ and $t = (n+1)T$, with n an integer number and T the tripole's rotation period. For example, the lobe denoted by A-S_1 is located in the ambient fluid and will be entrained into satellite S_1 after one period. The corresponding lobes for the cases $\epsilon = 0.2$ and $\epsilon = 0.3$ are shown in figure 14(*b,c*). It is obvious that the lobe area increases with increasing ϵ.

Note that every lobe is to be entrained into or detrained from a satellite, i.e. a satellite is involved in any mass exchange event, either with the central vortex or with

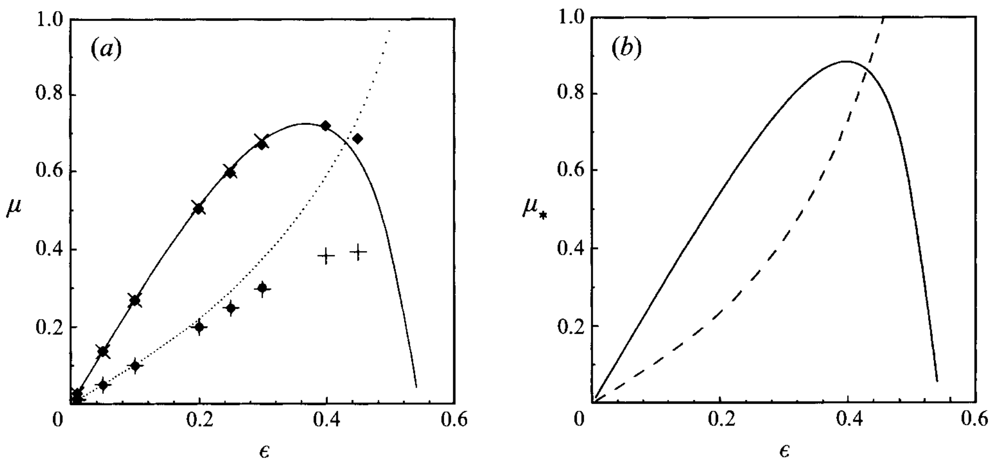

FIGURE 15. (*a*) Lobe area μ as a function of ϵ (expressed as a fraction of the area trapped by a satellite in the unperturbed case). The lobe areas of S_1 and S_2 are indicated by a solid line, those of C are indicated by a broken line. The lines represent Melnikov calculations and the symbols represent direct computations using the advection equations. (*b*) The corresponding exchange rate $\mu_* = \mu/T$, according to the Melnikov calculations.

the ambient fluid. For this reason it is natural to choose the area of a satellite in the unperturbed case ($\approx 2.054d^2$) as the unit area. Therefore, in what follows all areas are given as a fraction of this unit area. For example, the fluid area trapped by the central vortex, which is 58.5 % of that trapped by a satellite, is written simply as 0.585. In figure 15 the areas of the different entrainment lobes are given as a function of the initial asymmetry ϵ. The lines represent calculations using the Melnikov function, while the symbols give the result of direct numerical computations. Note that the ambient fluid exchanges equal amounts of mass with S_1 (diamonds) and with S_2 (crosses). Similarly, the central vortex exchanges equal amounts with S_1 (circles) and S_2 (pluses). This apparently surprising result can be explained by two properties: (i) the shape of a lobe depends on the time at which the Poincaré section is constructed, yet its area is conserved owing to the incompressibility of the velocity field, and (ii) the position of S_1 with respect to C at $t = nT$ is the same as the position of S_2 with respect to C at $t = (n + \frac{1}{2})T$. Property (i) establishes that any lobe of, say S_2, has a constant area, it thus follows from (ii) that the corresponding lobe of S_1 has the same area.

The lobe area for large ϵ is of order 1 (figure 15*a*). This does not mean that the whole core of S_1 will be substituted by new fluid coming from the exterior region or the central vortex C. A large fraction of the lobe will in fact be found within C and S_2 after one period. The mechanism for that is the intersection of the lobes corresponding to different regions. For instance, in figure 14(*a*) it can be seen that there is an intersection between lobes S_2-C and C-S_1; therefore, the fluid in that area will pass from satellite S_2 to S_1 in a single period.

4.1.3. *Long-time evolution of fluid particles*

The evolution of particles after several iterations of the Poincaré map is investigated in this section. Knowledge of the structure of the tangle helps to efficiently compute the evolution of particles. For small values of ϵ particles were placed in the lobe S_2-C, and for every period it is determined in which region each individual particle is

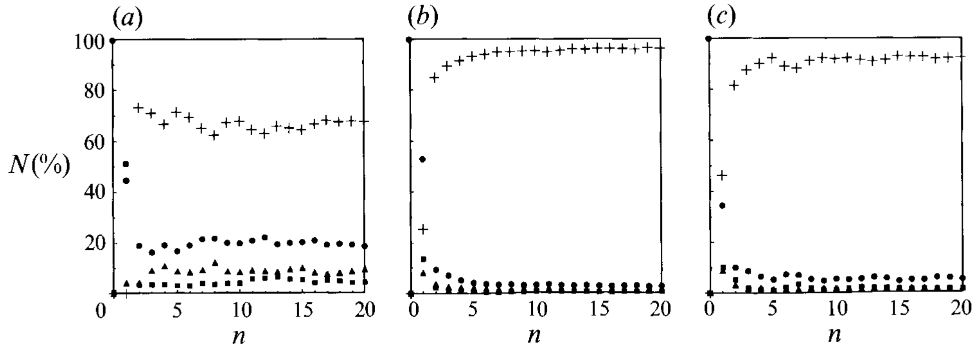

FIGURE 16. Percentage of particles (N) located in the ambient fluid (crosses), C (squares), S_1 (triangles), and S_2 (circles) after n periods, for different initial asymmetries: (a) $\epsilon = 0.05$; (b) 0.15; and (c) 0.25. A regular array of 3000 particles were initially located within the lobe that moves from S_2 to C during the first period.

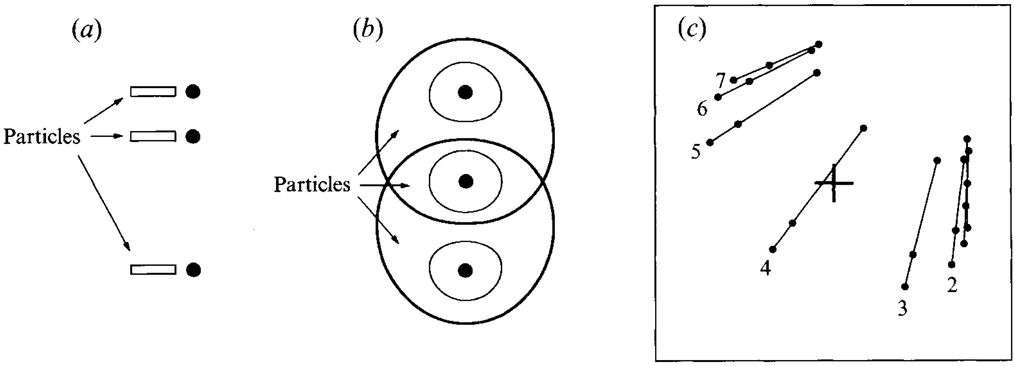

FIGURE 17. Initial location of tracers for 'brute force' calculations: (a) in the unmodulated – but asymmetric – case 1100 particles were located within each rectangle; (b) in the modulated – but initially symmetric – point-vortex tripole N particles were placed within each region determined by an arbitrarily chosen streamline and the separatrix ($N = 2000$ within each satellite and $N = 1400$ in the central vortex); and (c) linear-configuration events of a point-vortex tripole on a γ-plane (the numbers indicate the rotations of the satellites around the central vortex, i.e. the period).

located. The fraction of particles that are located in the different regions approaches a constant value (different in every region) as the number of periods grows (figure 16). In the range $0 < \epsilon < 0.25$ this effect is more rapidly achieved with growing ϵ, and in all cases it is completed approximately by period 15. Similar results are observed if the particles are located initially in another lobe, with the same percentage of particles as in figure 16 (within an accuracy of 3 % in our calculations) being located in different regions after 15–20 periods.

For ϵ close to the critical point (for both lower and larger values), the tangle has a complicated structure and the identification of the lobes becomes a laborious task. Therefore we turned to 'brute force' calculations for the study of particle motion in this range of the parameter ϵ. Now we are interested in the general structures that arise in the Poincaré section rather than in an accurate description of the motion of species through the different flow regions. For this purpose particles were located in rectangular arrays close to the point vortices (figure 17a) and their positions sampled after every quarter period (i.e. as the vortices are in a linear arrangement or as

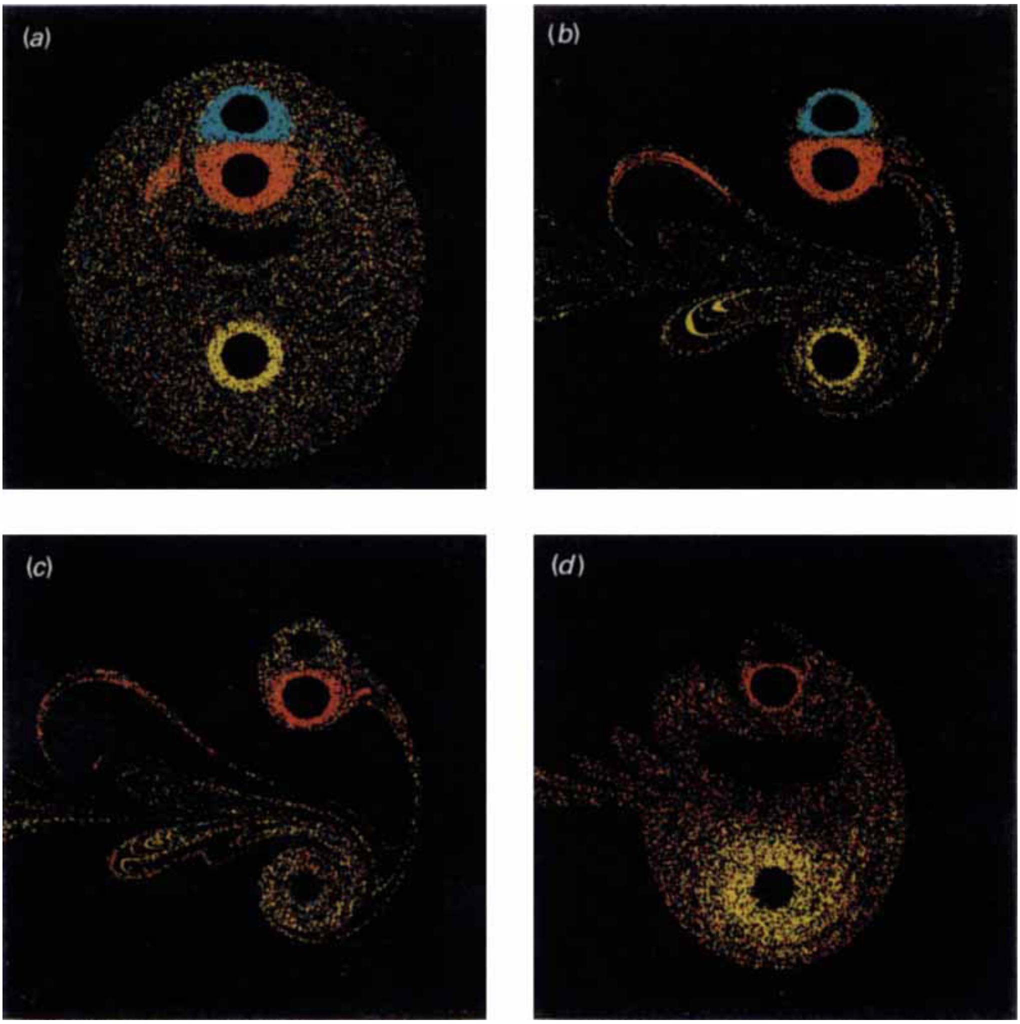

FIGURE 18. Positions of particles for a series of n iterations of the Poincare map for: (*a*) $\epsilon = 0.49$; (*b*) 0.54; (*c*) 0.56; and (*d*) 0.65. In (*a*) and (d) $n = 6, \ldots, 10$; and in (*b*) and (*c*) $n = 1, \ldots, 5$. 'Red' particles correspond to the central vortex, 'green' correspond to the satellite attached to the central vortex, and 'yellow' to the second satellite. For the number and initial position of particles see figure 17(*a*).

they form an isosceles triangle). However, we show here only the Poincare sections constructed at a linear configuration of the vortices.

In the range $0 < \epsilon < 0.5$ the structures governing the transport between the different vortex regions are qualitatively similar, but the size of the fluid region permanently trapped by the individual vortices (*cores*) decreases with increasing ϵ. A larger area, which surrounds the three vortices, is also permanently trapped by the tripole, and the fluid inside this region (but outside the cores) is strongly stirred. This extended region of trapped fluid has an almost circular shape for small values of ϵ, but it becomes more oval and decreases in size with growing ϵ. It reaches its minimum size for $\epsilon \approx 0.49$ (figure 18*a*). Here, a new closed region of unstirred fluid appears between the central vortex C and satellite S_2. A further increase of ϵ leads to the formation of small lobe-like structures at the rear of the oval region. These lobes greatly increase in size in the range $0.5 < \epsilon < 0.54$, resulting in an opening and destruction of the oval region (figure 18*b*).

The breakup of the oval region of trapped fluid around the tripole, as one approaches the critical value $\epsilon_c \approx 0.544$ from smaller or larger values of ϵ, is most likely the result of the velocity reaching its maximum value at ϵ_c. For ϵ close to ϵ_c the vortices translate almost as an equilateral triangle during a large fraction of each period. The fluid lost by any of the vortices during this phase is rapidly advected to the wake of the structure and cannot be recaptured when the central vortex makes a cycloid-like loop with one of the satellites.

Figure 18(*c*) shows that just beyond the critical point $\epsilon_c \approx 0.544$ the main features, such as the broad areas without particles between the couple C-S_1 and S_2 as well as the large lobe-like structures in the wake, are still observed in spite of the change of regime. However, close to the vortices an important change occurs: the regions of fluid permanently trapped by the satellites are almost completely absent (compare figures 18*b* and 18*c*). This results from the close approach of the like-signed vortices at $t = (n + \frac{1}{2})T$, as illustrated by the schematic figure 5(*c*) (compare it to figure 5*a*).

For even larger values of ϵ a new oval region of trapped fluid begins to form around the three vortices. The area of permanently trapped fluid around the distant satellite S_2 increases, while the area trapped by the coupled vortices C-S_1 decreases. This is illustrated in figure 18(*d*) for the case $\epsilon = 0.65$, where it can be seen that the core region of the 'independent' satellite S_2 has greatly increased, and a new region of unstirred fluid appears between the couple C-S_1 and satellite S_2. Lobe-like structures are present only in the upper half-plane, indicating that fluid escapes from this region but not from the lower half-plane.

It has been shown in §3.1 that for $\epsilon \rightarrow 1$, the three vortices translate like a dipolar vortex, with the couple C-S_1 effectively being substituted by a *virtual vortex* with the same net circulation of this asymmetric couple located at its centre of rotation. The validity of this analogy for the advection of passive tracers has also been tested. Several fluid regions that would be carried by the virtual dipole without change of size or shape have been placed in the velocity field of the three point vortices. For large values of the initial asymmetry ($\epsilon > 0.75$) the same area of fluid is carried by the tripole with almost no change of shape, a feature that is illustrated in figure 19 for the case $\epsilon = 0.8$. The fluid patches initially coincided with the (steady) streamlines of the virtual dipole, as indicated by the broken lines in figure 19. They were allowed to evolve with the three vortices during two periods, and the final positions of the curves are indicated by solid lines. It is clear that the separatrix has not been substantially deformed, and the lines surrounding satellite 2 have not changed either. Only lines close to the couple C-S_1 show a strong deformation. This result indicates that there is a fixed volume of fluid trapped by the tripole and that noticeable stirring takes place only in the vicinity of the couple C-S_1, which could be considered as a periodically perturbed dipole. Particle motion in this region can therefore be analysed as has been done for a dipole in an oscillating strain field (Rom-Kedar *et al.* 1990) or dipoles on the γ- and β-planes (Velasco Fuentes 1994; Velasco Fuentes *et al.* 1995).

4.2. *Advection by a modulated point-vortex tripole*

In §3.2 we showed that there are some parallels between the motion of an asymmetric tripole (with the point vortices having constant circulations) and a modulated tripole (being initially symmetric but having circulations that are functions of position). In both cases the point-vortex tripole drifts perpendicularly to the line at which the vortices align themselves and its mean speed increases with the amplitude of the

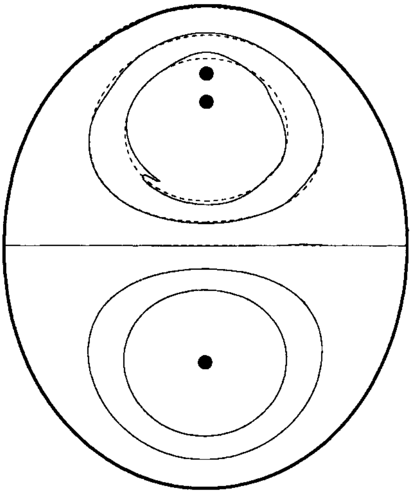

FIGURE 19. Advection of tracers in the dipole–monopole regime (here $\epsilon = 0.8$). The contours of the patches at $t = 0$ (broken lines) coincide with streamlines of the *virtual dipole* (see text). The shape of the contours after two periods is shown by solid lines.

perturbation (see §3.1). However, the asymmetric tripole moves in a fixed direction and its perturbation amplitude is constant, whereas the direction of motion and the perturbation amplitude of the modulated tripole change continuously.

The analogies exhibited by the motion of the vortices in these models might suggest that the advection of passive tracers also shows significant similitude. This was verified by numerical experiments performed at a few points of the parameter plane (γ_*, R), an example of which is discussed below (for the case $\gamma_* = 0.01$ and $R = 3$). The regions where the particles were located initially are indicated in figure 17(*b*). In the satellites the region is limited by the separatrices and the streamline located at a distance $0.2d$ along the y-axis, and in the central vortex the latter distance was $0.125d$. Particles were uniformly distributed along streamlines of the unperturbed stationary tripole. Particle positions are then plotted every period, i.e. every second linear-configuration event. In the Poincaré sections the positions are translated and rotated in such a way that the vortex C lies at the origin of the coordinate system and the satellites S_1 and S_2 are located at some distance on the y-axis. Figure 17(*c*) shows the real point-vortex positions after each period (the complete trajectories are shown in figure 7*a*).

As can be seen in figure 7(*b*), the tripole undergoes a growing phase between period 1 and 4. After each period the distance between the satellites increases while the central vortex C pairs with S_2. Owing to its increasing size, the tripole entrains fluid at its rear and advects it to its front (see figure 20*a*, which shows the particles at period 2). The asymmetry increases until period 4 and in every period entrainment of fluid occurs (figure 20*b*,*c*). After period 4 the asymmetry begins to decrease and lobe-like structures are formed at the rear, which indicates the detrainment of fluid, in this case not from the vortices themselves but from the oval region of stirred fluid that surrounds the tripole. At period 8 the tripole reaches its initial latitude and becomes (approximately) symmetric again. A new growing phase occurs between periods 8 and 12, and the process is repeated.

From the satellites themselves interior fluid is detrained during the first growing phase and the core of trapped fluid reduces in size, but after the first growing phase (periods 1–4) the core sizes do not change noticeably any further. The fluid patches

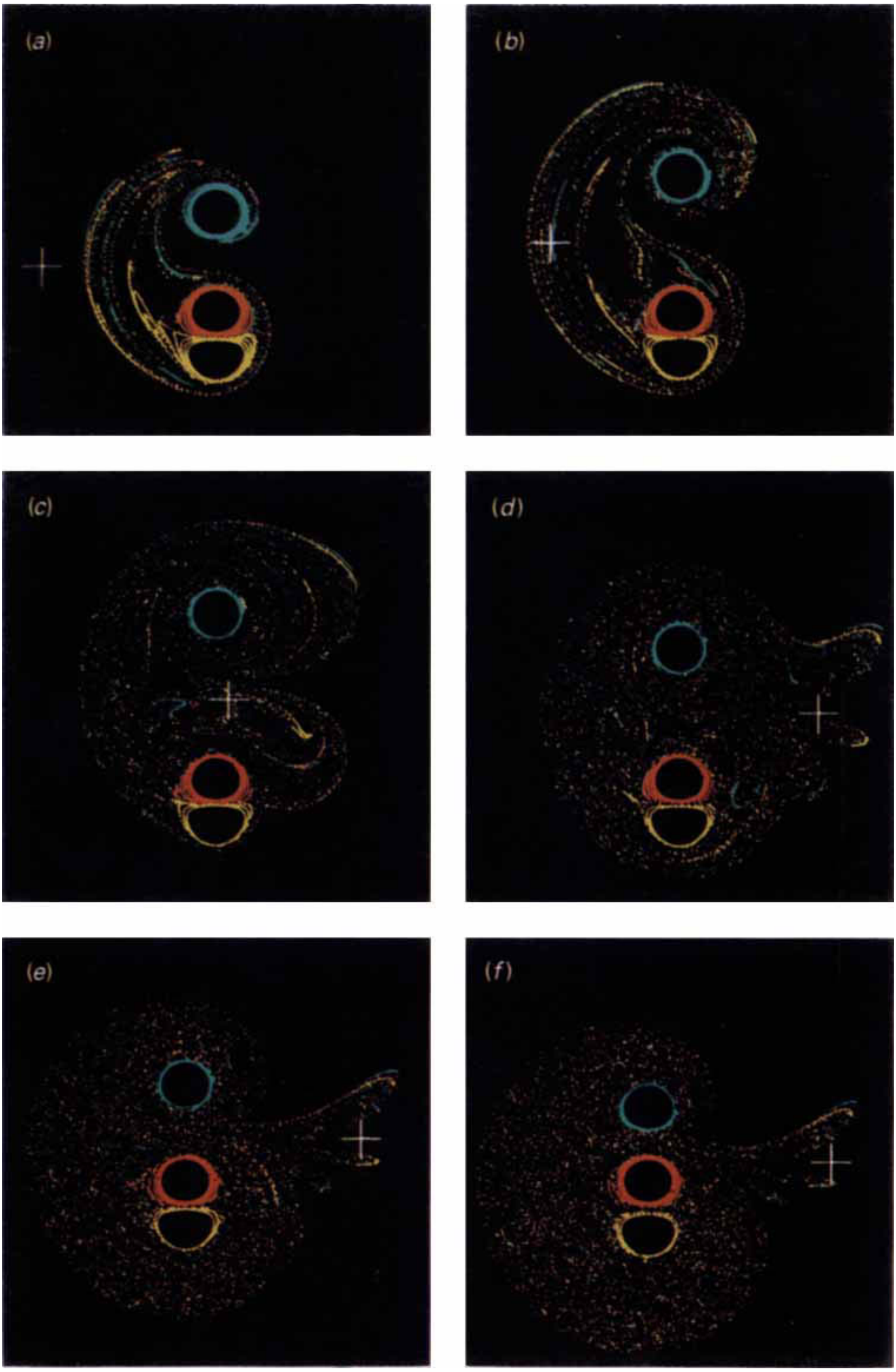

FIGURE 20. For caption see facing page.

ejected from the satellites are well stirred, remaining in the surroundings of the tripole for at least one tripole excursion.

This series of Poincaré sections illustrates a characteristic feature of the modulated tripole, namely that the distances between the vortices are not equal in two subsequent Poincaré sections. However, if the γ-effect is small (i.e. if $Rd\gamma_*/\kappa_0 \ll 1$ and $R = O(d)$) the difference between those distances is small and the vortices' circulations remain approximately constant, in which case the evolution during any period is mainly determined by the configuration at the beginning of that period. This argument suggests that the series of Poincaré maps obtained from a single initial condition in the parameter plane (γ_*, R), approximately corresponds with a series of Poincaré sections obtained in the asymmetric (but non-modulated) case for some range of the parameter ϵ.

4.3. *Experimental observations*

For the analysis of transport in the experimental situation we return to the experiment shown in figure 1. The distribution of dye at some particular instants in the evolution is analysed. These instants are chosen as those at which linear ($\theta = \pi$) or isosceles-triangle ($a = b$) configurations occur.

The dye used for visualization was placed originally in the outer ring of the monopolar vortex. Therefore, as the tripole is formed, most of the dye becomes concentrated in the satellites, while the central vortex consists of undyed fluid. This was done because one satellite is always involved in the exchange of fluid, either with the central vortex or with the ambient fluid. Fluid can pass from one satellite to the other through the central vortex, and from the latter to the ambient fluid through one of the satellites.

Time $t = 0$ is defined as the instant at which the generation of the tripole was completed, and the rotation period of the table ($T = 11.1$ s) is taken as the unit of time. In figure 21(*a*) one can see a fairly symmetric structure, with the three vortices well aligned and S_1 and S_2 closely attached to C. However, the tripole soon becomes asymmetric and although at $t = 3.2T$ the three vortices are again linearly arranged (figure 21*b*), S_2 has separated from C, while S_1 remains attached to the central vortex, forming a dipole-like structure. Bands of fluid (both dyed and undyed) connect this couple with the monopole at the front of the tripole (which moves to the left in the pictures), while fluid is being entrained between the couple and the monopole S_2 at the rear of the tripole. Owing to its asymmetry the couple C-S_1 moves back and collides with S_2 at $t = 5T$ (figure 21*c*). A large ring of undyed fluid surrounds satellite S_2 at this stage. The central vortex C changes partner and moves away with vortex S_2, forming a compact couple. As the structure reaches a new linear configuration at $t = 7.7T$ the amplitude of the asymmetry has grown noticeably (figure 21*d*). The band of fluid connecting the couple with the monopole is thicker and contains larger lobes of ambient fluid, and a large amount of fluid is being entrained at the rear side of the tripole. The couple C-S_2 moves back and collides with vortex S_1 at $t = 10.4T$

FIGURE 20. Advection by the modulated point-vortex tripole on the γ-plane: the graphs show the positions of particles in different Poincaré sections in a single numerical experiment. (*a*) $n = 2$, (*b*) 3, (*c*) 4, (*d*) 5, (*e*) 6, (*f*) 7. The calculations were performed for $R = 3$, $\gamma_* = 0.01$. The vortex trajectories are shown in figure 7(*a*), the positions of the vortices at periods 2–7 are shown in figure 17(*c*) and the number and initial position of particles are indicated in figure 17(*b*). 'Red' particles were located initially within the central vortex, and 'green' and 'yellow' particles within each satellite, respectively. The crosses indicate the position of the pole (or tank centre).

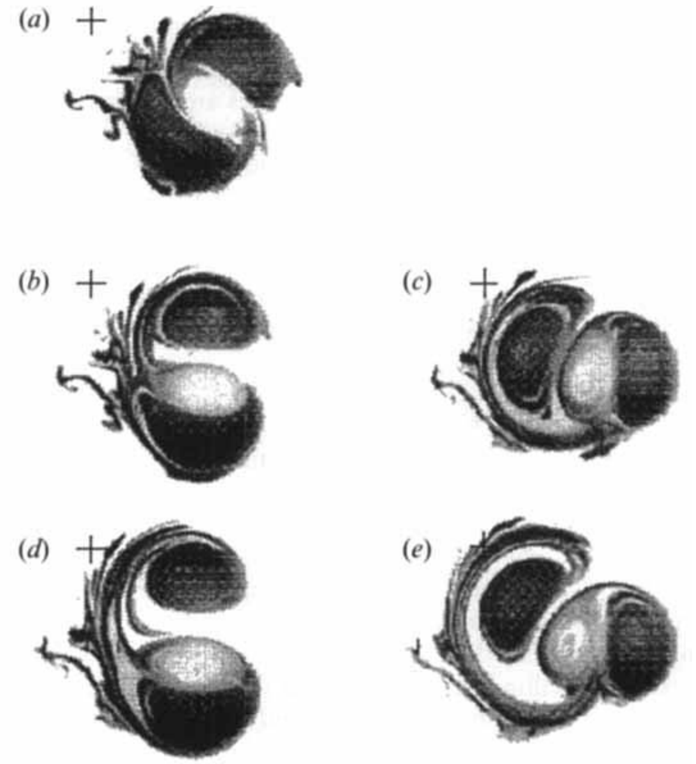

FIGURE 21. Plan-view of the experimental tripolar vortex shown in figure 1. Linear or isosceles-triangle configurations are observed to occur at (*a*) $t = 0$, $3.2T$ (*b*), $5T$ (*c*), $7.7T$ (*d*) and $10.4T$ (*e*), where $T = 11.1$ s is the rotation period of the table. The crosses indicate the position of the tank centre.

(figure 21*e*). The kink of the tripole is larger than in frame (*c*), and the ring of ambient fluid surrounding S_1 is also larger than the ring around S_2 in (*c*).

The same modulated point-vortex model used to simulate the motion of the vortex centres (figure 10*b*) is used now to simulate the advection of fluid patches. The initial contours of these patches were chosen to be the separatrices of the unperturbed tripole. As in the experiment described above the contours are plotted when a linear or an isosceles-triangle configuration occurs. In that sense the series correspond with one another, although not exactly in time (see §3.3). All the main features observed in the laboratory experiment can be observed in the simulation, namely formation of bands of interior fluid at the front and entrainment of ambient fluid at the rear, with the amount of entrained fluid increasing as time progresses (compare figure 22*b* with 22*d* or figure 22*c* with 22*e*).

5. Conclusions

We have studied the unsteady motion of a tripolar vortex on a rotating free-surface fluid. It has been observed in the laboratory that a tripole generated off-centre is initially symmetric: the three vortices are located on a straight line and the satellite vortices are equally separated from the central vortex. However, the structure soon becomes asymmetric, which results in the emergence of a misalignment of the vortices and the pairing of the central vortex with one of the satellites. The tripole

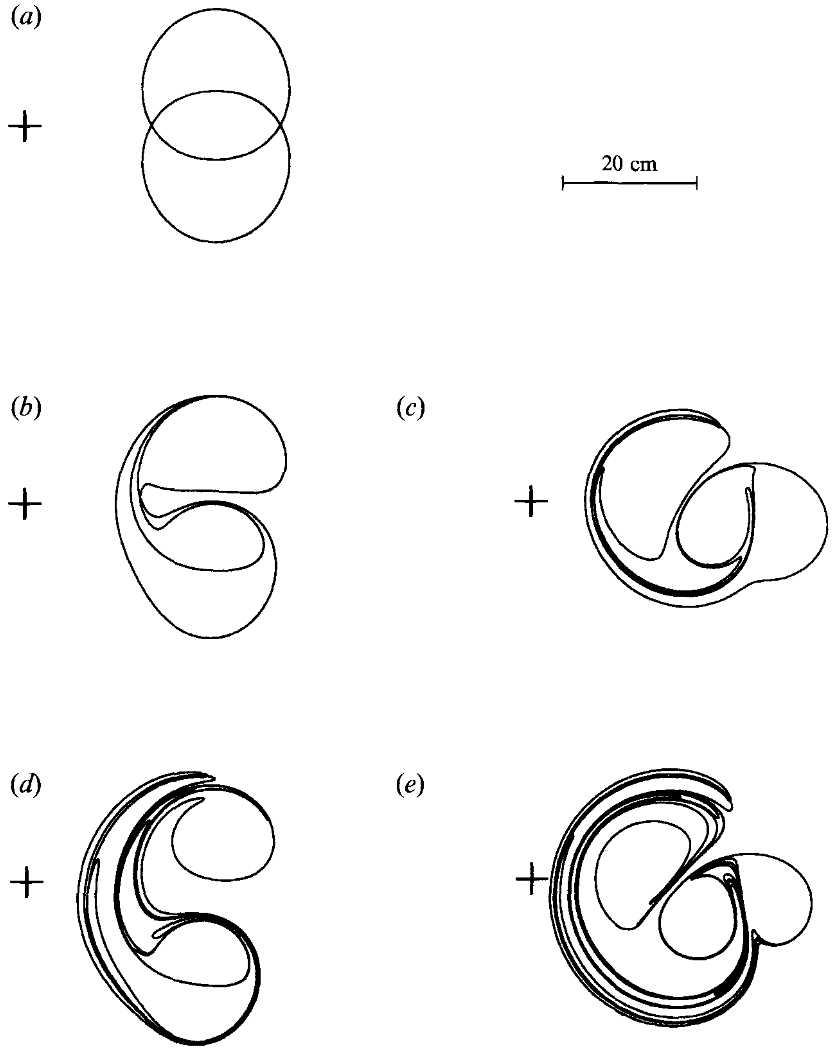

FIGURE 22. Numerical simulation of the evolution of fluid initially trapped by the modulated point-vortex tripole. Calculations were performed using the same initial conditions as those in the experiment shown in figure 21 and results are shown as the point vortices reach the corresponding configuration. The contours of the patches initially trapped by the symmetric tripole are shown at (*a*) $t = 0$, $5.8T$ (*b*), $8.5T$ (*c*), $12.6T$ (*d*) and $15.8T$ (*e*); with T the timescale used in figure 21.

then translates and rotates quasi-periodically, with the central vortex pairing in turn with each satellite. This time-dependent behaviour leads to shedding of mass from the satellites and stretching and folding of the detrained fluid.

A non-modulated point-vortex tripole shows a similar time-dependent behaviour. As in the experiments this asymmetric structure has net linear momentum, but in contrast with the observations the motion is periodic and the asymmetries have a constant amplitude. The motion of particles in the velocity field of this point-vortex tripole was studied using the 'dynamical-systems' approach, and it was found that for all values of the perturbation parameter $\epsilon \neq 0$ chaotic particle motions appear and fluid is exchanged between the different flow regions. The amount of mass exchanged during one period increases with increasing ϵ. Except for values of ϵ close to the critical value ($\epsilon_c \approx 0.544$), the translating tripole carries a large area of stirred fluid.

The squeezing and stretching of fluid columns due to the parabolic free surface of the fluid (the topographic equivalent of the γ-plane) was proposed as a mechanism for the enhancement of the asymmetry and the translation of the tripole. The hypothesis was tested using a point-vortex tripole modulated on the basis of conservation of potential vorticity on the (topographic) γ-plane. It was found that an initially symmetric point-vortex tripole becomes asymmetric owing to the modulation. In addition to the rotational motion of the satellites around the central vortex, the structure as a whole translates towards the centre of the tank. The rotation period of the satellites around the central vortex is not constant, and the perturbation amplitudes increase as the tripole shifts centrewards. As a consequence, the advection of particles cannot be studied with a single two-dimensional map – as in the non-modulated case – but with a series of maps. Numerical calculation of such series shows that during the phase of growing perturbation the tripole entrains mass and efficiently stirs a large region of fluid, which is also carried by the tripole during the phase of decreasing perturbation. The vortex trajectories as well as the advection of fluid masses computed using this simple modulated point-vortex model show a remarkable agreement with the experiments observations.

There is a remarkable similarity between the flow field of a tripolar vortex and the field due to an elliptical patch of uniform vorticity (i.e. a Kirchhoff vortex), when they are viewed in their respective co-rotating frames. In such frames both velocity fields possess three centres of rotation and two stagnation points as in figure 13(*a*). As a consequence, if a small perturbation is imposed on either system the resultant advection patterns will be similar. This can be easily verified by comparing, for instance, the flow around an asymmetric point-vortex tripole (for $\epsilon \ll \epsilon_c$) with the flow around a Kirchhoff vortex embedded in a weak linear strain, i.e. with the flow around a Kida vortex (Polvani & Wisdom 1990). However, the advection patterns produced by a strongly asymmetric tripole are qualitatively very different from the patterns produced by a Kida vortex with an intense background flow. In the tripolar vortex the size of the chaotic region is comparable to the tripole's size, whereas in the Kida vortex the chaotic region can be much larger than the elliptical vortex (Polvani & Wisdom 1990).

We thank students Rob van Gansewinkel and Roel Vanneer for their contribution to the numerical simulations. We also thank the referees for their valuable comments on an earlier version of this paper. O.U.V.F. gratefully acknowledges financial support from the Netherlands Foundation for Fundamental Research on Matter (FOM).

REFERENCES

AREF, H. 1979 Motion of three vortices. *Phys. Fluids* **22**, 393–400.

AREF, H. 1984 Stirring by chaotic advection. *J. Fluid Mech.* **143**, 1–21.

AREF, H. 1989 Three-vortex motion with zero total circulation: Addendum. *Z. Angew. Math. Phys.* **40**, 495–500.

BATCHELOR, G. K. 1967 *An Introduction to Fluid Dynamics*. Cambridge University Press.

CARNEVALE, G. F., KLOOSTERZIEL, R. C. & HEIJST, G. J. F. VAN 1991 Propagation of barotropic vortices over topography in a rotating tank. *J. Fluid Mech.* **233**, 119–139.

CARTON, X. J., FLIERL, G. R. & POLVANI, L. M. 1989 The generation of tripoles from unstable axisymmetric isolated vortex structures. *Europhys. Lett.* **9**, 339–344.

Carton, X. J. & Legras, B. 1994 The life-cycle of tripoles in two-dimensional incompressible flow. *J. Fluid Mech.* **267**, 53–82.

Flór, J. B., Govers, W. S. S., Heijst, G. J. F. van & Sluis, R. van 1993 Formation of a tripolar vortex in a stratified fluid. *Appl. Sci. Res.* **51**, 405–409.

Gröbli, W. 1877 *Specielle Probleme über die Bewegung geradliniger paralleler Wirbelfäden.* Zürcher und Furrer, Zürich.

Heijst, G. J. F. van & Kloosterziel, R. C. 1989 Tripolar vortices in a rotating fluid. *Nature* **338**, 369–371.

Heijst, G. J. F. van, Kloosterziel, R. C. & Williams, C. W. M. 1991 Laboratory experiments on the tripolar vortex in a rotating fluid. *J. Fluid Mech.* **225**, 301–331.

Heijst, G. J. F. van & Velasco Fuentes, O. U. 1994 Unsteady behaviour of a tripolar vortex on a γ-plane. In *Modelling of Oceanic Vortices* (ed. G. J. F. van Heijst). Verhandelingen Koninklijke Nederlandse Akademie van Wetenschappen. North-Holland.

Kono, J. & Yamagata, T. 1977 The behaviour of a vortex pair on the beta plane. *Proc. Oceanogr. Soc. Japan* **36**, 83–84 (in Japanese).

Legras, B., Santangelo, P. & Benzi, R. 1988 High-resolution numerical experiments for forced two-dimensional turbulence. *Europhys. Lett.* **5**, 37–42.

Leith, C. E. 1984 Minimum enstrophy vortices. *Phys. Fluids* **27**, 1388–1395.

Nof, D. 1990 Modons and monopoles on a γ-plane. *Geophys. Astrophys. Fluid Dyn.* **52**, 71–87.

Novikov, E. A. 1976 Dynamics and statistics of a system of point vortices. *Sov. Phys. JETP* **41**, 937–943.

Orlandi, P. & Heijst, G. J. F. van 1992 Numerical simulation of tripolar vortices in 2D flow. *Fluid Dyn. Res.* **9**, 179–206.

Pedlosky, J. 1979 *Geophysical Fluid Dynamics.* Springer.

Pingree, R. D. & LeCann, B. 1992 Three anticyclonic slope water oceanic eddies (swoddies) in the southern Bay of Biscay in 1990. *Deep-Sea Res.* **39**, 1147–1175.

Poincaré, H. 1893 *Théorie des Tourbillons.* Leçons Professees Pendant le Deuxième Semestre 1891–1892 (ed. G. Carré). Paris.

Polvani, L. M. & Wisdom, J. 1990 On chaotic flow around the Kida vortex. In *Topological Aspects of Fluid Mechanics* (ed. H. K. Moffatt & A. Tsinober). Cambridge University Press.

Rom-Kedar, V., Leonard, A. & Wiggins, S. 1990 An analytical study of transport, mixing and chaos in an unsteady vortical flow. *J. Fluid Mech.* **214**, 347–394.

Rott, N. 1989 Three-vortex motion with zero total circulation. *Z. Angew. Math. Phys.* **40**, 473–494.

Sutyrin, G. G., Hesthaven, J. S., Lynov, J. P. & Rasmussen, J. J. 1994 Dynamical properties of vortical structures on the beta-plane. *J. Fluid Mech.* **268**, 103-131.

Synge, J. L. 1949 On the motion of three vortices. *Can. J. Maths* **1**, 257–270.

Velasco Fuentes, O. U. 1994 Propagation and transport properties of dipolar vortices on a γ plane. *Phys. Fluids* **6**, 3341–3352.

Velasco Fuentes, O. U. & Heijst, G. J. F. van 1994 Experimental study of dipolar vortices on a topographic β-plane. *J. Fluid Mech.* **259**, 79–106.

Velasco Fuentes, O. U., Heijst, G. J. F. van & Cremers, B. E. 1995 Chaotic advection by dipolar vortices on a β-plane. *J. Fluid Mech.* **291**, 139–161.

Wiggins, S. 1992 *Chaotic Transport in Dynamical Systems.* Springer.

Zabusky, N. J. & McWilliams, J. C. 1982 A modulated point-vortex model for geostrophic, β-plane dynamics. *Phys. Fluids* **25**, 2175–2182.